

## Near-critical behavior of the Zhong-Zhang model

J. H. Lowenstein <sup>\*</sup>

Department of Physics, New York University, 726 Broadway, New York, New York 10003, USA



(Received 13 July 2023; accepted 4 January 2024; published 5 February 2024)

The Zhong-Zhang (ZZ) model is a one-degree-of-freedom dynamical system describing the motion of an insulating plate of length  $d$  floating on the upper surface of a convecting fluid, with locking at the boundaries. In the absence of noise, the system away from the boundaries is described by linear differential equations with a delay time  $\tau$ . The  $d, \tau$  plane consists of two domains separated by a critical curve. For asymptotically long times, subcritical orbits approach a nontrivial periodic attractor, while the supercritical ones tend to a stationary state at the origin. We investigate near-critical behavior using a modified fourth-order Runge-Kutta integration scheme. We then construct a piecewise analytic decomposition of the periodic attractor, which makes possible a far higher level of accuracy. Our results provide solid evidence for an asymptotic power-law approach to criticality of several observables. The power laws are fed back to determine the piecewise-analytic structure deep into the near-critical regime. In an Appendix, we explore the effect of introducing noise using modified order-3/2 Kloeden-Platen-Schurz stochastic integration, following several observable quantities through the near-critical parameter domain.

DOI: [10.1103/PhysRevE.109.025102](https://doi.org/10.1103/PhysRevE.109.025102)

### I. INTRODUCTION

To investigate the effects of a mobile insulating plate on turbulent Rayleigh-Benard convection, with an eye to obtaining a better understanding of the geophysical phenomenon of continental drift, Zhang and Libchaber [1] and Zhong and Zhang [2,3] conducted a series of small-scale experiments set up as in Fig. 1. In the absence of the plate, a uniform temperature difference  $\Delta T$  is maintained between the bottom and top of the fluid in a rectangular container of length  $D$ , producing a turbulent flow with two counter-rotating convective rolls. An insulating plate on the top fluid surface distorts the heat flow, giving rise to asymmetric frictional forces and motion of the plate.

The asymptotic long-time behavior of the coupled plate-fluid system in the experiments of Refs. [1–3] was found to depend in a simple way on the length  $d$  of the plate in units where  $D = 1$ . For  $d$  less than a critical value  $d_{\text{crit}}$ , there were approximately periodic sojourns at the boundaries of the cell, while for larger  $d$ , the motion rapidly tended to rest at the center of the cell. In a subsequent paper [4], Zhong and Zhang developed a simple one-degree-of-freedom system which accounts for the principal experimental results. In this model, hereafter referred to as the ZZ model, the state of the system is given by a pair  $(x, y)$ , where  $x$  is the distance of the plate center from the center of the cell, and  $y$  represents the position of the convective upwelling (see Fig. 1).

When the plate is away from the boundary, i.e.,  $|x| < L = (1 - d)/2$ , the system obeys a pair of linear first-order delay differential equations (DDE),

$$\begin{aligned}\dot{x}(t) &= a[x(t) - y(t)] - bx(t - \tau), \\ \dot{y}(t) &= c[x(t) - y(t)],\end{aligned}\quad (1)$$

where

$$\begin{aligned}a(d) &= [2v_0 + \theta(1 - d)]/(d + g), \\ b(d) &= d\theta/(d + g), \\ c(d) &= d\beta,\end{aligned}$$

and  $v_0, g, \beta, \theta$ , and  $\tau$  are empirically determined constants. When the plate is stationary at one of the boundaries, i.e.,  $x = \pm L$ , the upwelling position  $y$  continues to evolve according to the second of the equations.

In Eqs. (1),  $v_0$  and  $\theta$  parametrize the assumed linear dependence of the convective flow speed on the uncovered surface area, while  $g$  is the ratio of the thickness  $\lambda$  of the viscous boundary layer adjacent to the plate to the width  $w$  of the latter, multiplied by a geometric factor  $\gamma$ . The velocity of the upwelling position is assumed to be proportional, by a factor  $d\beta$ , to its displacement from the center of the plate. Finally, the delay time  $\tau$  is the response time of the fluid circulation speed to a change in the exposed surface area. For a precise interpretation of the constants and their empirical determination, the reader is referred to Sec. III and Appendix A of Ref. [4].

Following Ref. [4], we fix  $v_0, g, \beta, \theta$  at the values (with times expressed in seconds, lengths in units of  $D$ )

$$v_0 = 0.015, \quad \theta = 0.075, \quad g = 1.8, \quad \beta = 0.017, \quad (2)$$

and consider  $d$  and  $\tau$  as the parameters of the model. Specification of  $x(t)$  as a continuous function of  $t$  for times  $-\tau \leq t \leq 0$ , as well as  $y(0)$  leads to a unique solution  $(x(t), y(t))$  for all nonnegative times. Numerical explorations for different values of  $d$  and  $\tau$  reveal the existence of a convex *critical curve*  $\mathcal{C}$  in the  $d, \tau$  plane which separates it into two regions, a *subcritical* region I in which the system alternates between unlocked and locked motion, and a *supercritical* region II in which the motion, after a threshold time depending on the initial conditions, the motion is entirely free of locking. In

<sup>\*</sup>john.lowenstein@nyu.edu

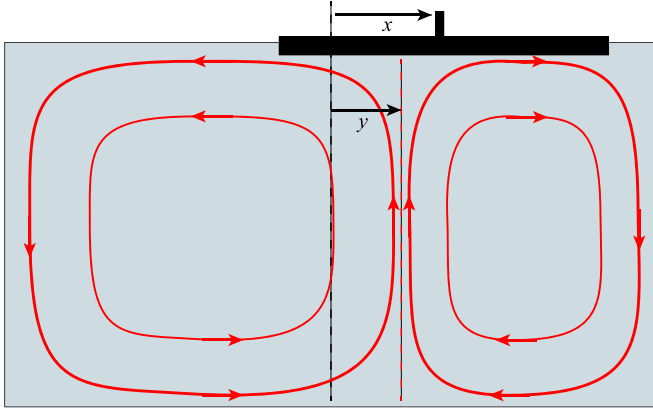


FIG. 1. Side view of the experimental setup of Refs. [1–3]. An insulating plate of length  $D$  moves on the surface of a convective fluid with two rolls. The horizontal positions of the plate center and the fluid upwelling are assigned coordinates  $x$  and  $y$ , respectively.

each region the asymptotic motion converges to an attractor. In I this is a topological circle, while in II it is a single point, namely  $(0,0)$ . On the critical curve, there are infinitely many concentric elliptical attractors. A phase diagram derived from the model equations in Sec. III is shown in Fig. 2.

As pointed out in Ref. [4], the initial value problem for the linear DDE for boundary-free motion in the ZZ model can be solved using Laplace transforms [5]. This analysis reveals the critical behavior at  $d = d_{\text{crit}}$  for given delay parameter  $\tau$ , and allows one to study the asymptotic approach to the fixed point at the origin for  $d_{\text{crit}} < d < 1$ . The principal aim of the current investigation is to obtain an equally thorough understanding of the subcritical solutions of the ZZ model equations, especially with regard to the approach to criticality.

The need for a more precise study of the subcritical orbits stems from the fact that their asymptotic behavior is not accurately described, even for short time intervals, by the asymptotic elliptical arcs of the boundary-free DDE. The DDE certainly apply between visits to the boundaries, but the initial conditions are reset with each such visit. This puts into question the existence and precise characterization of an

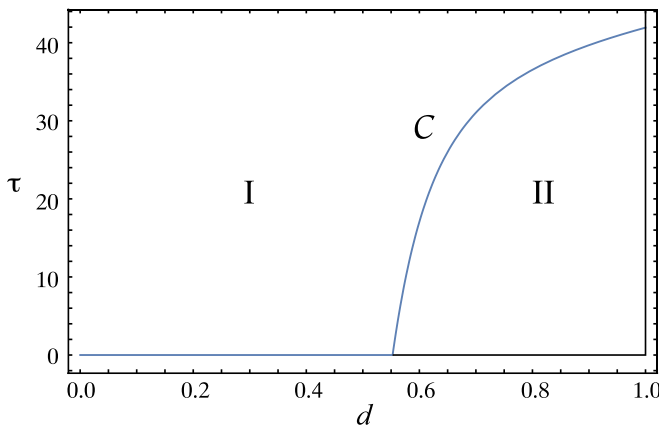


FIG. 2. Phase diagram in the  $d, \tau$  parameter plane, with critical curve  $C$ , derived in Sec. III below. The corresponding plot (Fig. 11) in Ref. [4] is not accurate for  $d > 0.8D$ .

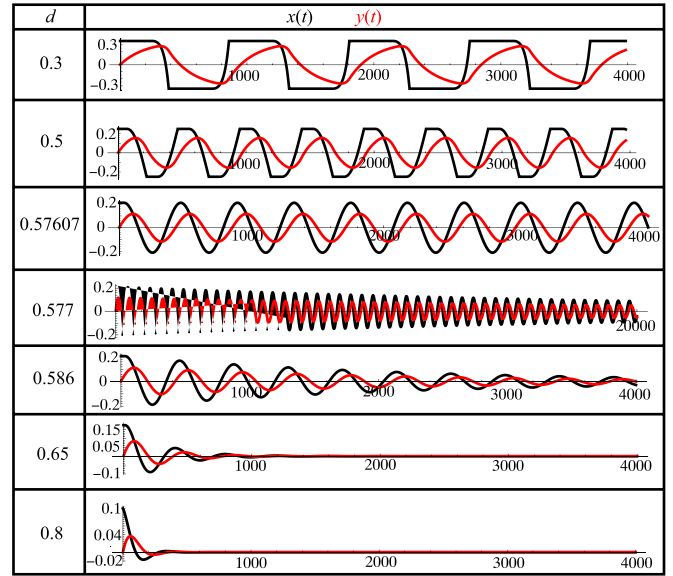


FIG. 3. Plots of  $x(t)$  (black) and  $y(t)$  (red) for  $\tau = 10$ ,  $0.3 < d < 0.8$ . In each case, the plate is released from rest at  $x = L$  with  $y(0) = 0$ .

attracting periodic orbit for subcritical parameter values, even though the experimental and numerical results of Ref. [4] strongly suggest that such an attractor exists.

Our investigation begins with a concise review, in Secs. II and III, of some of the main results of Ref. [4], with some important refinements needed for later sections. In particular, we introduce an efficient numerical integration scheme, namely fourth-order Runge-Kutta updating adapted to the presence of delay terms and locking/unlocking transitions, which is designed to provide sufficient accuracy for the study of extremely long orbits near criticality. The plots of  $x(t)$  and  $y(t)$  in Figs. 3–6 are obviously not new, but are included to give the reader an adequate introduction to further, more abstract, developments.

The discussion of solutions of the boundary-free DDEs in Sec. III also covers ground already treated in Ref. [4], again with the motivation of providing an introduction to key features. An important result here is the phase diagram of Fig. 2, which differs from that derived in Ref. [4] in the

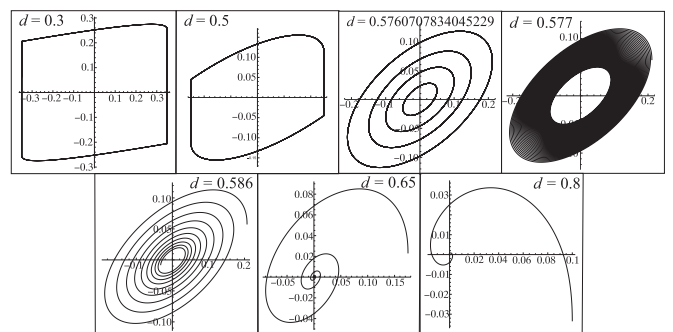


FIG. 4. Plots of  $x(t)$  vs  $y(t)$  for  $\tau = 10$ ,  $0.3 < d < 0.8$ . Several different initial conditions were used for  $d = d_{\text{crit}}$ . For other values,  $x(t) = L, -\tau \leq t \leq 0$ , and  $y(0) = 0$ .

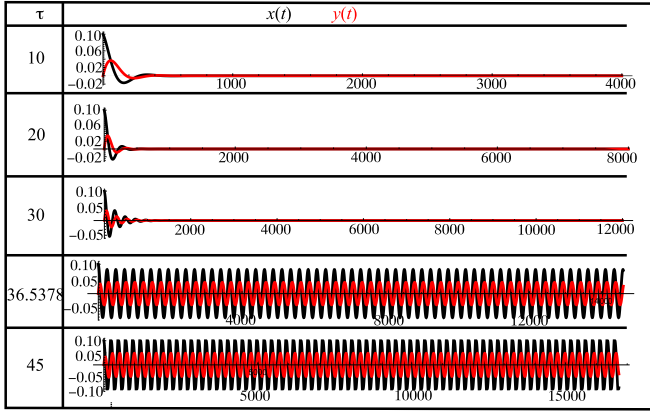


FIG. 5. Plots of  $x(t)$  (black) and  $y(t)$  (red) for  $d = 0.8$ ,  $10 < \tau < 45$ .

large- $d$  regime. This section also contains a description, going beyond that of Ref. [4], of the limit-cycle behavior of the strictly critical orbits, taking into account the subtleties of the initial-value problem in the presence of nonzero delay.

Our main results are found in Secs. IV–VI below, where we explicitly construct piecewise analytic periodic attractors for all but a zero-measure set of resonant  $\tau, d$  values in region I. Each piece is of duration less than or equal to the delay time  $\tau$ , and consists of a finite linear combination of expressions  $t^k$  and  $t^j e^{(a-c)t}$ , with coefficients linked to those of other pieces by linear recursion and continuity relations. Having obtained accurate approximate solutions using our numerical integrations, we then use the results as the starting point for a high-precision construction of the piecewise analytic attractor. This method gets us sufficiently close to the critical curve that we can determine with some confidence the asymptotic behavior of the oscillation period and the locking time as we approach the critical bifurcation. This is sufficient to ascertain the piecewise analytic structure of the attractor in the extreme near-critical regime.

While the main results of the article concern the deterministic ZZ model, it is also of interest to explore how the intricate near-critical behavior is transformed by the introduction of noise, consistent with the actual conditions in the laboratory

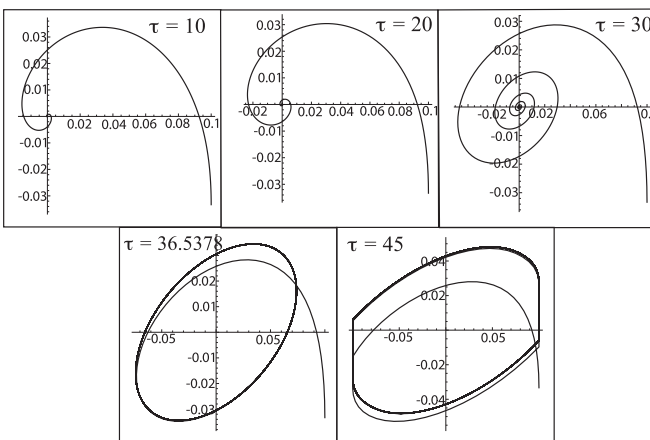


FIG. 6. Plots of  $x(t)$  vs  $y(t)$  for  $d = 0.8$ ,  $10 < \tau < 45$ .

experiments. Not surprisingly, the noisy model, simulated in Appendix C using a modified order-3/2 Kloeden-Platen-Schurz stochastic integration scheme [6], has no sharp critical bifurcation. Rather one finds a broad critical zone in which various observables associated with boundary-locking tend continuously to zero.

Similar results were previously obtained by Huang, Zhong, Zhang, and Mertz [7,8] for a stochastic ZZ model without time delay and with the parameter  $g$  in Eqs. (1) set equal to zero. With these assumptions, the authors were able to reformulate the model within the powerful framework of stochastic variational inequalities, originally developed by Bensoussan *et al.* [9,10] to model elastoplastic oscillators. Applied to the ZZ model with noise, the authors were able to derive and solve Kolmogorov equations for the transition probabilities and thus calculate a number of statistical properties of the observables.

The success of the ZZ model in capturing some of the key features of partially covered Rayleigh-Benard convection has been followed up by a number of recent advances in achieving a deeper understanding of the phenomenon and its relation to geophysical continental drift. While the present work, as well as that of Refs. [7,8], has concentrated on the ZZ model itself, others [11–13] have been able to obtain a more nuanced description of the plate-fluid coupling and of the evolution of the turbulent fluid with more general assumptions about its size and geometry, and with closer attention to the observed features of plate tectonics.

## II. NUMERICAL SOLUTION OF THE EQUATIONS OF MOTION

We begin our study of the ZZ model by examining numerical solutions of the DDE for various values of plate length  $d$  and time-delay  $\tau$ , with the parameters  $v_0, \theta, \beta$ , and  $g$  fixed at the values (2). We break up the integration range into intervals

$$I_n = [n\tau, (n + 1)\tau], \quad n = -1, 0, 1, 2, \dots, N - 1,$$

and then subdivide each  $I_n$  into  $M$  time steps of duration  $\Delta t = \tau/M$ . To obtain a unique solution for  $t \geq 0$ , we specify  $y(0)$  and  $x(t)$  for all times of  $I_{-1}$ . For each successive  $I_n, n = 0, 1, 2, \dots, N - 1$ , we calculate the  $x, y$  orbit using fourth-order Runge-Kutta updating with time increment  $\Delta t$ , treating the  $x$  values of  $I_{n-1}$  as a forcing function. The Runge-Kutta algorithm requires the delayed  $x$  values at interval midpoints, and these are supplied using five-point Lagrange interpolation.

We now carry out two sequences of numerical integrations of the ZZ system to illustrate the features discussed qualitatively in the previous section. First, we fix the delay time at  $\tau = 10$  (a horizontal line in Fig. 2) and consider a sequence of plate length  $d$  increasing from  $d = 0.3$  in region I to  $d = 0.8$  in region II, crossing the critical curve  $C$  at  $d = 0.57607\dots$  Plots of  $x(t)$  and  $y(t)$  are displayed in Fig. 3, while the corresponding orbits in the  $x, y$  plane are shown in Fig. 4. In both the subcritical and critical examples, the initial portion of the orbit reflects arbitrarily chosen initial conditions, while the long-time behavior shows convergence to a unique attractor. In the critical case, the elliptical attractor is nonunique.

Our second sequence of examples starts at  $d = 0.8, \tau = 10$  and proceeds along a vertical line in the diagram, from  $\tau = 10$  in region II to  $\tau = 45$  in region I, crossing  $C$  at  $\tau = 36.5378$ .

The results are shown in Figs. 5 and 6. The qualitative behavior seen in the first sequence is once again observed, in the opposite order.

As a preliminary check on the precision of our numerical integrations, we measured the asymptotic *locking time* (during which the plate is locked at a boundary) and *flight time* (during which it is in motion between boundaries) for fixed  $\tau = 10$ ,  $d = 0.3$  and varying choices of the time step  $\Delta t$  and total time  $t_{\text{tot}}$ . We found that for fixed  $t_{\text{tot}}$  the error scaled as  $(\Delta t)^4$ , as expected. However, for fixed  $\Delta t$ , convergence to an attractor was quite rapid. For example, with  $\Delta t = 0.0025$ , the difference in the  $f$  or  $l$  values between  $t_{\text{tot}} = 1000$  and  $t_{\text{tot}} = 500\,000$  was smaller than  $10^{-90}$ . Note, however, that this attractor is not identical to the exact attractor, although it presumably converges to it for  $\Delta t$  tending to zero. For  $t_{\text{tot}} = 20\,000$ , the values of  $f$  and  $l$  coincide with those obtained analytically in Sec. V in their first 19 digits. Reducing  $\Delta t$  by a factor of 32 improves the precision to 24 digits.

In Ref. [3], the change in dynamical behavior occurring as  $d$  passes through  $d_{\text{crit}}$  is described as a *Hopf bifurcation*, a well known scenario in low-dimensional nonlinear dynamical system theory (see Ref. [14], Sec. 2.8). For such a system, as a control parameter  $\lambda$  approaches its critical value  $\lambda_{\text{crit}}$  from (say) above, one has an attracting fixed point at the origin and a repelling periodic orbit surrounding it, while after  $\lambda$  passes through  $\lambda_{\text{crit}}$  the origin becomes a repeller with an attracting periodic orbit surrounding it.

The behavior of the ZZ system near  $d = d_{\text{crit}}$  bears a certain resemblance to a Hopf-bifurcating system, specifically in the change of stability of the origin precisely at criticality. However, there are important differences. For example, the supercritical ZZ system is essentially linear, with no unstable periodic orbit present. Moreover, the amplitude of the stable attractor of the Hopf system tends smoothly to zero while approaching the bifurcation from below, whereas the amplitude of the  $x$ -oscillation of the ZZ system remains constant at  $L$  right up to  $d = d_{\text{crit}}$ . The precise asymptotic behavior of the attractor will become apparent only after our detailed analysis of Secs. IV–VI.

### III. BOUNDARY-FREE MOTION FOR LONG TIMES

Before proceeding to our analysis of the approach to criticality, it is essential to establish the phase diagram of Fig. 2 and specifically the bifurcation curve  $\mathcal{C}$  with high precision. Following Ref. [4], we will exploit the convenient circumstance that the phase diagram, the critical curve, and the region-II long-time behavior of the ZZ model all coincide with those of the simpler linear model in which the DDEs (1) apply to the entire  $x, y$  plane. The nonlinear, boundary dependent, behavior in Region I requires a completely different approach, as we will see in Secs. IV–VI.

Again following [4], we note that DDEs (1) are relatively simple examples of a broad class of linear DDEs analyzed by Bellman and Cooke [5], and we will make use of their results in the following. The key idea is to expand in terms of exponential solutions

$$(x(t), y(t)) = (x_0(z), y_0(z))e^{zt}.$$

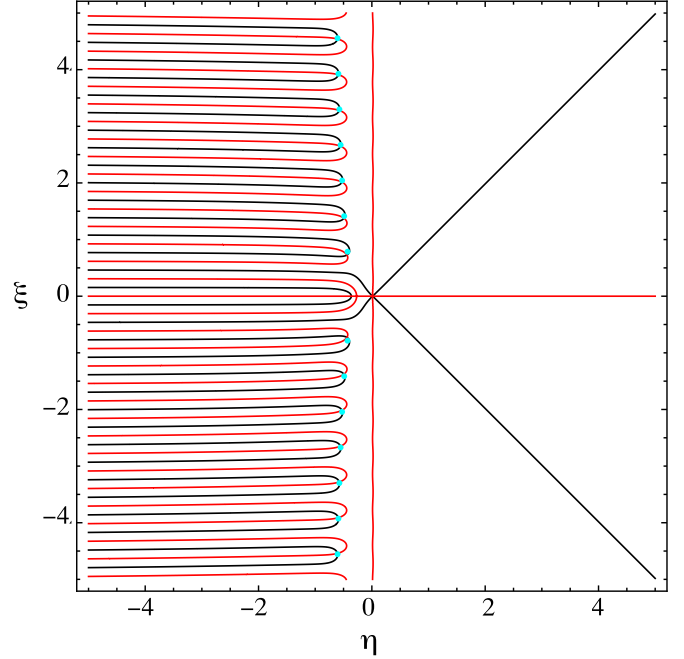


FIG. 7. Zeros of  $\chi(z)$  for  $\tau = 10$ ,  $d = 0.3$  (subcritical). Curves where  $\text{Re}(\chi(z)) = 0$  are shown in black, those where  $\text{Im}(\chi(z)) = 0$  in red. The approximate roots from Eq. (5) are included as cyan dots.

The DDE implies the eigenvalue equation

$$\begin{pmatrix} z - a + be^{-\tau z} & a \\ -c & z + c \end{pmatrix} \begin{pmatrix} x_0(z) \\ y_0(z) \end{pmatrix} = 0.$$

For a nontrivial solution, the complex number  $z = \eta + i\xi$  must satisfy the *characteristic equation*

$$\chi(z) = z^2 + (c - a)z + b(z + c)e^{-\tau z} = 0,$$

that is,

$$\eta^2 - \xi^2 + (c - a)\eta + b e^{-\tau\eta}[(\eta + c) \cos \tau\xi + \xi \sin \tau\xi] = 0, \tag{3}$$

$$2\eta\xi + (c - a)\xi + b e^{-\tau\eta}[-(\eta + c) \sin \tau\xi + \xi \cos \tau\xi] = 0. \tag{4}$$

Figure 7 locates the zeros of  $\chi(\eta + i\xi)$  in the  $\eta, \xi$  plane for  $d = 0.3$ ,  $\tau = 10$ . They lie at the intersections of the curves  $\text{Re}(\chi(z)) = 0$  (black) and  $\text{Im}(\chi(z)) = 0$  (red). To resolve the zeros near the origin, we zoom in with Fig. 8.

We note that the two roots near the origin have positive real parts, corresponding to spiraling outward in the  $x, y$  plane. The remaining roots are well separated from the origin, forming complex conjugate chains with all real parts less than some negative bound, corresponding to exponential contraction. The approximate locations of these roots can be obtained [5] by keeping only the leading large- $z$  terms in the characteristic equation,

$$ze^{\tau z} + b = 0,$$

that is,

$$z = \tau^{-1} \ln(-b/z).$$

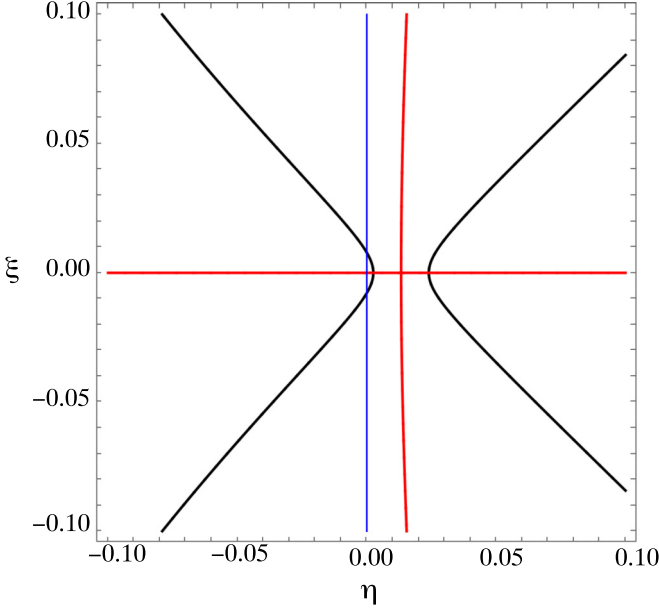


FIG. 8. Zoom of the central portion of Fig. 7. The imaginary axis  $\eta = 0$  is a thin blue line.

Asymptotically, the roots  $z_n$  form complex-conjugate chains with

$$\begin{aligned} \text{Im}(z_n) &= \pm \tau^{-1} \left( \frac{\pi}{2} + 2\pi n \right), \\ \text{Re}(z_n) &= \tau^{-1} \ln \left( \frac{b\tau}{\frac{\pi}{2} + 2\pi n} \right), \quad n = 1, 2, \dots \end{aligned} \quad (5)$$

The location of the infinitely many roots of the characteristic function for  $\tau = 10$ ,  $d = 0.3$ , is typical for region I in Fig. 2. The critical case for  $\tau = 10$ , lying on the critical curve  $\mathcal{C}$ , is shown in Fig. 9, while supercritical and subcritical examples for  $d = 0.8$  are presented in Fig. 10. In each case, the two dominant roots near the origin determine the asymptotic behavior.

To calculate the critical curve  $\mathcal{C}$  with high precision, we set  $\eta = 0$  in Eqs. (3) and (4),

$$-\xi^2 + b(d)[c(d) \cos \tau \xi + \xi \sin \tau \xi] = 0,$$

$$(c(d) - a(d))\xi + b(d)[-c(d) \sin \tau \xi + \xi \cos \tau \xi] = 0,$$

solving numerically for  $d$  and  $\xi$ . For  $\tau = 10$ , shown in Fig. 9, this yields

$$d = d_{\text{crit}} = 0.57607078340452299,$$

$$\xi = \pm i\omega, \quad \omega = 0.014667757818838299.$$

The asymptotic long-term behavior of a typical solution with critical  $d$  is thus motion on an ellipse with angular frequency  $\omega$ . The nonleading part of the solution falls off exponentially, with the rate dominated by the root of the characteristic equation on the negative real axis. This can be obtained by setting  $\xi = 0$  in Eq. (3),

$$\eta^2 + [c(d) - a(d)]\eta + b(d)e^{-\tau\eta}[\eta + c(d)] = 0,$$

to obtain

$$\eta = -0.28386336427345445.$$

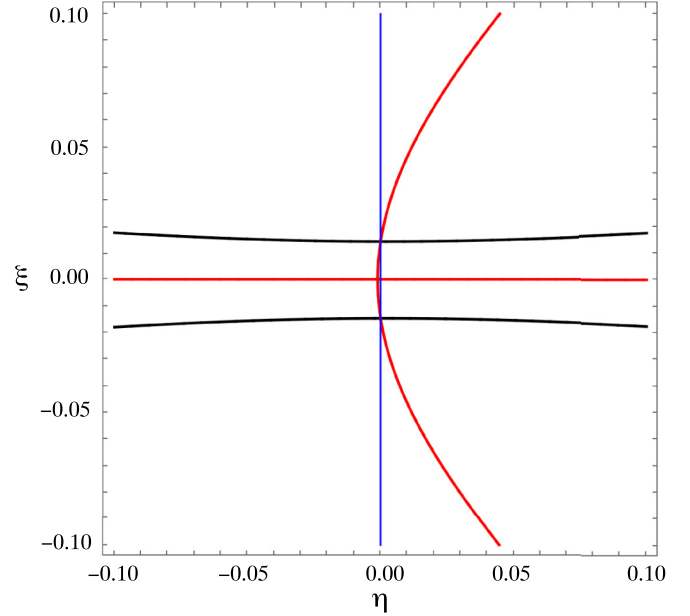


FIG. 9. Zeros of  $\chi(z)$  for  $\tau = 10$ ,  $d = 0.5760707834045229$  (critical) lie at intersections of the black and red curves on the imaginary axis (blue).

The asymptotic behavior thus emerges rapidly during a single oscillation period  $2\pi/\omega$ .

The position  $\eta$  of the subdominant root on the negative real axis can be calculated for arbitrary  $\tau$  and  $d$  using the above equation. The results for selected  $\tau$  values is shown in Fig. 11.

In Ref. [5] it is shown that for arbitrary continuously differentiable  $x(t)$  on the initial interval  $-\tau \leq t \leq 0$ , a solution of the DDE exists for all  $t \geq 0$  in the form of a convergent sum of exponential solutions,  $e^{z_k t}$ ,  $z_k$  a root of the characteristic function. To illustrate, let us imagine a thought-experiment for the case  $\tau = 10$ ,  $d = d_{\text{crit}}$ . To set up simple initial conditions, we start with the upwelling close to  $y = 0$  and hold the plate fixed at  $x = x_0$ ,  $0 < x_0 \leq L$  by placing a bar across the fluid surface at  $x = x_0$ . The plate presses against the bar until some time  $t > \tau$  when  $y$  reaches the value  $(1 - b/a)x_0$ , at which point  $\dot{x}$  decreases through zero and the plate starts moving toward the boundary at  $x = -L$ . The bar is now removed, having served only to set up the initial conditions. The solution of the DDE is

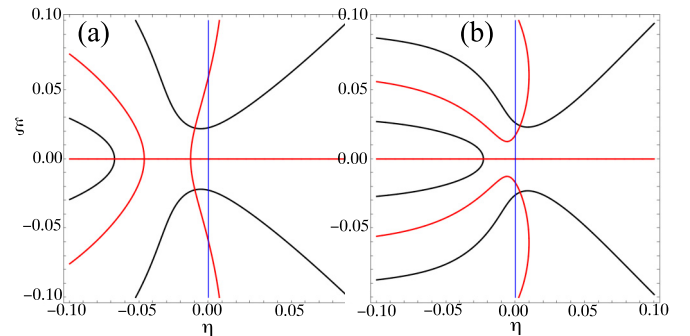


FIG. 10. Zeros of  $\chi(z)$  for  $d = 0.8$  and (a)  $\tau = 20$  (supercritical) and (b)  $\tau = 45$  (subcritical) lie at intersections of the black and red curves, with negative and positive real parts, respectively.

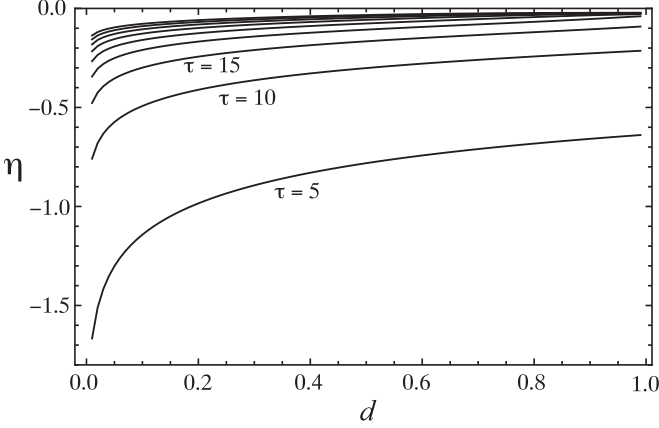


FIG. 11. Position of subdominant root of the characteristic equation on the negative real axis, for  $0.01 \leq d \leq 0.99$ ,  $\tau = 5n$ ,  $n = 1, 2, \dots, 9$ .

now a superposition of exponentials  $\exp z_n t$ , where  $z_n$  are the roots of the characteristic function  $\chi(z)$ . For asymptotically long times, only the contributions from the conjugate roots on the imaginary axis,  $z_{\pm 1}$ , are relevant.

Using the Laplace transform method of Ref. [5] applied to our release-from-rest initial conditions, we find the asymptotic solution

$$\begin{pmatrix} x_{\text{as}}(t) \\ y_{\text{as}}(t) \end{pmatrix} = F(z_{+1})e^{z_{+1}t} + F(z_{-1})e^{z_{-1}t},$$

where  $F(z)$  is given by

$$\frac{x_0 e^{-\tau z}}{\chi'(z)} \begin{pmatrix} z+c & -a \\ c & z-a+be^{-\tau z} \end{pmatrix} \begin{pmatrix} 1 - \frac{b}{z}(1 - e^{-\tau z}) \\ 1 - \frac{b}{a} \end{pmatrix}.$$

The asymptotic orbit is an ellipse with maximum  $x$  coordinate given by

$$x_{\text{max}} = x_{\text{as}}(t_{\text{max}}), \quad t_{\text{max}} = \frac{1}{|z_{+1}|} [\arg F(z_{+1}) + j\pi], \quad j \in \mathbb{Z}.$$

Inserting  $\tau = 10$ ,  $d = d_{\text{crit}}$ , we get

$$x_{\text{max}} = 0.9991135304636472 \dots x_0.$$

The initial conditions of our thought-experiment were used, with four different  $x_0$  values, to generate the critical orbits shown in Fig. 4. In one case, we chose  $x_0 = L$ , where the asymptotic ellipse comes close (but not quite!) to grazing the boundary.

The same method used in our critical example also allows for an exact calculation of the asymptotic  $x, y$  orbits for any  $\tau, d$  with  $d \geq d_{\text{crit}}(\tau)$ , provided one uses the prescribed release-from-rest initial conditions. The same cannot be said for subcritical orbits. Such a system may never actually experience the complex-exponential asymptotic behavior, since locking with the boundaries will periodically reset the initial conditions of the DDE. For such parameter values, a different sort of analysis will be given in the next section.

#### IV. PERIODIC ATTRACTOR FOR LOCKING TIME $l \geq \tau$

We now begin a systematic study of motion on the subcritical periodic attractor. For given  $\tau$ , we define  $d_*$  as the

value of  $d$  such that the residence time at  $x = \pm L$ , the *locking time*  $l$ , is precisely the delay time  $\tau$ . For arbitrary  $d \leq d_*$ , at the moment of unlocking at  $x = \pm L$ , the  $\dot{x} = 0$  condition implies  $y = (1 - b/a)L$ . This allows us to construct explicitly the part of the orbit which travels from  $x = L$  to  $x = -L$  as a piecewise analytic periodic function of time. As we will see in Secs. V and VI, this characterization persists for almost all  $d$  values between  $d_*$  and  $d_{\text{crit}}$ , but the construction acquires considerable additional complexity. Before taking that on, we proceed with the details of the construction for  $d \leq d_*$ .

We begin by computing the orbit for the first  $\tau$  seconds of its flight, where Eqs. (1) take the forms

$$\dot{x}(t) = a(x(t) - y(t)) - bL, \quad \dot{y}(t) = c(x(t) - y(t)),$$

with initial conditions

$$x(0) = L, \quad \dot{x}(0) = 0, \quad y(0) = \left(1 - \frac{b}{a}\right)L.$$

One easily verifies the solution

$$\begin{aligned} x_1(t) &= x_{1,0} + x_{1,1}t + x_{1,0}^e e^{\alpha t}, \\ y_1(t) &= y_{1,0} + y_{1,1}t + y_{1,0}^e e^{\alpha t}, \quad \alpha = a - c, \end{aligned}$$

where

$$\begin{aligned} x_{1,1} = y_{1,1} &= \frac{bcL}{\alpha}, \quad y_{1,0}^e = -\frac{bc^2L}{\alpha a^2}, \quad x_{1,0}^e = \frac{a}{c}y_{1,0}^e, \\ y_{1,0} &= (1 - b/a)L - y_{1,0}^e, \quad x_{1,0} = y_{1,0} + \frac{1}{c}y_{1,1}. \end{aligned}$$

Extending the orbit all the way to arrival, at time  $f$ , at the left-hand boundary,  $x = -L$ , we find a continuous solution of the DDE of the following form. For

$$(n - 1)\tau \leq t \leq n\tau, \quad n = 0, 1, \dots, N, \quad (N - 1)\tau < f \leq N\tau,$$

we have, writing  $s = t - (n - 1)\tau$ ,

$$\begin{aligned} x(t) = x_n(s) &= \sum_{k=0}^n x_{n,k} s^k + \sum_{k=0}^{n-1} x_{n,k}^e s^k e^{\alpha s}, \\ y(t) = y_n(s) &= \sum_{k=0}^n y_{n,k} s^k + \sum_{k=0}^{n-1} y_{n,k}^e s^k e^{\alpha s}. \end{aligned}$$

In what follows we will refer to linear combinations of terms  $s^k$ ,  $k = 0, \dots, n$ , and  $s^k e^{\alpha s}$ ,  $k = 0, \dots, n - 1$ , as *basis functions of degree  $n$* . Starting with

$$x_0(s) = L, \quad y_0(0) = (1 - b/a)L, \quad (6)$$

the basis function coefficients for successive segments of the flight are obtained by recursive application of a sequence of linear equations. For  $n = 1, 2, \dots, N$ , we have

$$x_{n,n} = y_{n,n} = \frac{bc}{n\alpha} x_{n-1,n-1}, \quad (7)$$

$$y_{n,n-1}^e = -\frac{bc}{(n-1)\alpha} x_{n-1,n-2}^e, \quad (n \neq 1), \quad (8)$$

$$x_{n,n-1}^e = \frac{a}{c} y_{n,n-1}^e, \quad (n \neq 1). \quad (9)$$

Moreover, for fixed  $n \geq 2$  and  $k = n - 1, \dots, 1$ ,

$$y_{n,k} = \frac{1}{k\alpha} [bcx_{n-1,k-1} + k(k+1)y_{n,k+1}], \quad (10)$$

$$x_{n,k} = y_{n,k} + \frac{k+1}{c} y_{n,k+1}, \quad (11)$$

and for fixed  $n \geq 3$  and  $k = n - 2, \dots, 1$ ,

$$y_{n,k}^e = -\frac{1}{k\alpha} [bcx_{n-1,k-1}^e + k(k+1)y_{n,k+1}^e], \quad (12)$$

$$x_{n,k}^e = \frac{a}{c} y_{n,k}^e + \frac{k+1}{c} y_{n,k+1}^e. \quad (13)$$

All of the above relations are consequences of the DDE, rewritten in the form

$$\ddot{y}_n(t) = \alpha \dot{y}_n(t) - bcx_{n-1}(t - \tau), \quad (14)$$

$$x_n(t) = y_n(t) + \frac{1}{c} \dot{y}_n(t), \quad n = 1, \dots, N. \quad (15)$$

To complete the recursion, the constant terms are fixed by continuity of  $x(t)$  and  $y(t)$  at  $t = (n - 1)\tau$ :

$$y_{n,0}^e = \frac{c}{\alpha} \left[ x_n(0) - y_n(0) \right] - \frac{1}{c} (y_{n,1} + y_{n,1}^e), \quad (16)$$

$$x_{n,0}^e = \frac{a}{c} y_{n,0}^e + \frac{1}{c} y_{n,1}^e, \quad (17)$$

$$y_{n,0} = y_n(0) - y_{n,0}^e, \quad (18)$$

$$x_{n,0} = y_{n,0} + \frac{1}{c} y_{n,1}. \quad (19)$$

Note the recursive structure of the above relations: each coefficient is a linear combination of previously calculated coefficients. In the following we will denote the sequence of recursion Eqs. (7)–(19) as

$$\xi_n = \mathcal{R}(\xi_{n-1}, \xi_n(0)), \quad (20)$$

where

$$\xi_n(s) \stackrel{\text{def}}{=} (x_n(s), y_n(s)).$$

Note that, from Eq. (7), the  $n = 1$  recursion uses only  $x_{0,0} = L$ .

Continuity relations for time-derivatives at the points  $t = n\tau$  can easily be derived from the DDE and the continuity of  $x(t)$ ,  $y(t)$ , and  $\dot{x}(t)$  at  $t = 0$ . Specifically, at  $t = n\tau$ , the first  $n + 1$  derivatives of  $x(t)$  and the first  $n + 2$  derivatives of  $y(t)$  are continuous. While remaining piecewise analytic, the orbit becomes progressively smoother as time progresses, until the collision with the wall at the *flight time*  $f$  produces a discontinuity in  $\dot{x}(t)$ .

To illustrate our construction, we plot, in Fig. 12, the four-segment continuous, piecewise analytic, orbit for  $\tau = 35$ ,  $d = 0.3$ , and  $0 \leq t \leq f$ .

Now let us follow the orbit beyond the arrival at

$$x = x_N(f) = -L, \quad y = y_{\text{arr}} = y_N(f). \quad (21)$$

While the right-hand side of the  $\dot{x}$  DDE remains negative, the plate remains locked at the boundary, with  $x(t) = -L$  and the upwelling center moving leftward according to

$$\dot{y} = -c(L + y),$$

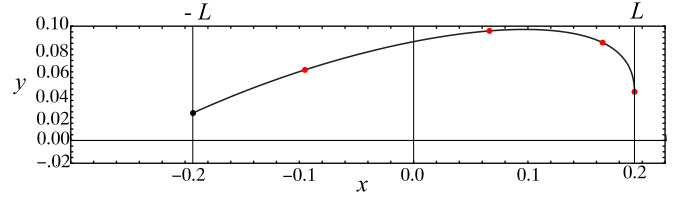


FIG. 12. Flight portion of the orbit for  $\tau = 35$ ,  $d = 0.3$ . The flight starts from rest at  $x = L = 0.2$  and ends with the sudden locking at  $x = -L = -0.2$  (black dot). Red dots are placed where  $t = 0, \tau, 2\tau, 3\tau$ .

with the solution

$$y(t) + L = (y_{\text{arr}} + L)e^{-c(t-f)}.$$

After a locking time

$$l = \frac{1}{c} \ln \frac{a(L + y_{\text{arr}})}{bL}, \quad (22)$$

the upwelling center reaches  $y = -(1 - b/a)L$ , where the right-hand side of the  $\dot{x}$  DDE changes sign, signaling unlocking of the plate. Since the unlocking values of  $x$  and  $y$  are just the negatives of the initial departure coordinates, and since the DDE's are invariant under inversion in the  $x, y$  plane, we see that the return trip of the plate from  $x = -L$  to  $x = L$  is just the calculated orbit for  $0 \leq t \leq f$  inverted through the origin. The plate collides (and locks) at the right-hand boundary at  $t = 2f + l$  and the upwelling center continues rightward according to

$$\dot{y} = c(L - y).$$

The orbit returns to its initial point at time

$$T = 2f + 2l, \quad (23)$$

and then repeats the cycle periodically. To calculate  $f, l$ , and  $T$  for given  $d \leq d_*$ , we solve Eq. (21) numerically and substitute into Eqs. (22) and (23). The results for  $\tau = 10$  are plotted in Figs. 13 and 14.

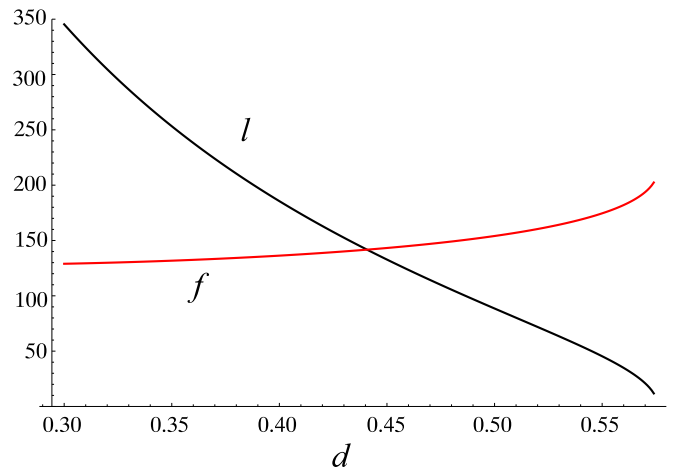


FIG. 13. Flight time  $f$  and locking time  $l$  for  $\tau = 10$ ,  $d \leq d_* = 0.57453138926606815$ .

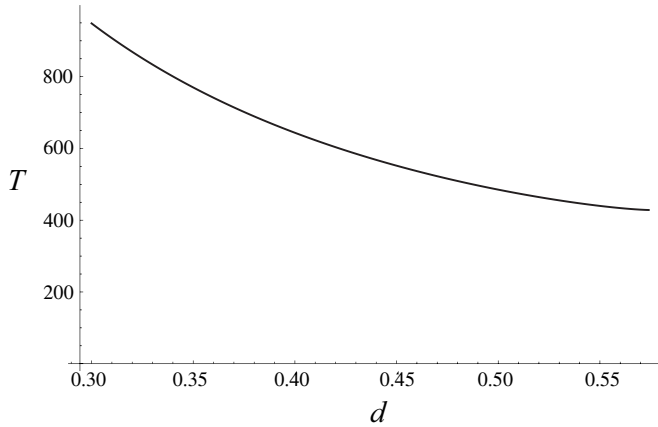


FIG. 14. Period  $T$  of the attractor for  $\tau = 10$ ,  $d \leq d_*$ .

To calculate  $d_*$  as a function of  $\tau$ , we solve the equation

$$l(\tau, d_*) = \tau$$

numerically for  $d_*$ , using the secant method. We have achieved 40-digit precision for all the quantities  $f, d_*, l, T$ . This level of precision is made possible by the use of analytic recursion relations, thus avoiding the truncation errors of numerical integration techniques. The function  $d_*(\tau)$  is plotted in Fig. 15. A new phase diagram in the  $d, \tau$  plane is shown in Fig. 16, where the subcritical region I has been separated into two regions, Ia and Ib, by the curve  $C'$  on which  $d = d_*(\tau)$ .

**V. FIRST STEP BEYOND  $d = d_*$**

Having studied in detail the piecewise analytic periodic orbits of region Ia, let us now venture into the more complex region Ib where  $d_* < d < d_{crit}$ . The numerical experiments of Sec. II suggest that the qualitative behavior as a nonlinear dynamical system does not change drastically as one enters this region from below. We continue to have two periodic orbits, a repeller fixed at  $x = y = 0$  and a nontrivial periodic attractor composed of alternating flights and locking intervals.

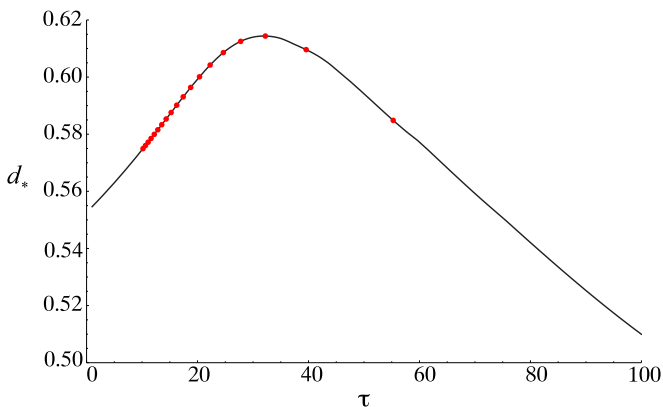


FIG. 15. Plate lengths  $d_*(\tau)$  for  $0 \leq \tau \leq 100$ . The red dots indicate the points where the number of analytic pieces of the orbit increases by one, starting with the jump from two to three at the rightmost dot.

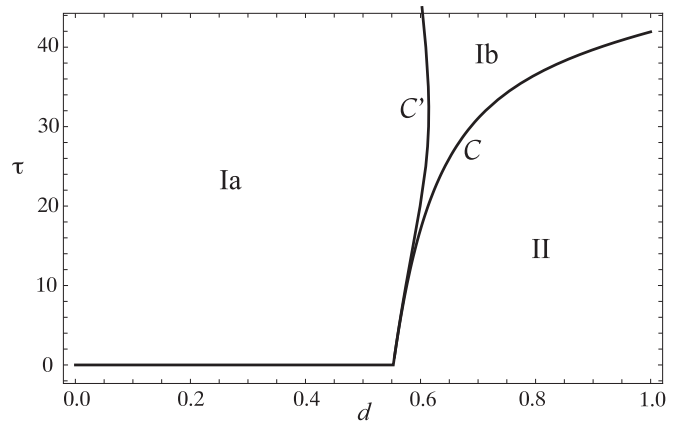


FIG. 16. New phase diagram in  $d, \tau$  parameter space. The curve  $C'$  corresponds to  $d = d_*(\tau)$ , for which the locking time  $l$  is equal to the delay time  $\tau$ .

Our goal is an explicit piecewise-analytic decomposition of the attracting orbit.

To begin our discussion, let us consider the case  $\tau = 35$ , chosen because of its relatively short flight time (less than  $4\tau$ ). The relevant range of  $d$  values is

$$(d_*, d_{crit}) = (0.6135270200322760, 0.7645997799038989).$$

For  $d < d_*$ , one can show that, as in the example of Fig. 12, the flight contains successive time intervals  $S_n = [(n - 1)\tau, n\tau]$ ,  $n = 1, 2, 3, 4$ , on which the orbit is represented by a pair of basis functions  $(x_n(s), y_n(s))$  of degree  $n$ , linked by the recursion function  $\mathcal{R}$  and continuity relations. We want to explore the possibility that the periodic attractor for  $d$  just above  $d_*$  also has a piecewise basis-function decomposition. Once again, the basis functions for intervals  $S_1, S_2, S_3, S_4$  would be linked by  $\mathcal{R}$ , but now there would be interspersed intervals  $S_5, S_6, S_7, S_8$  of length  $\delta_1 = \tau - l$  (as in Fig. 17). We conjecture that these, too, correspond to basis-function solutions of the DDE of degrees 5,6,7,8, respectively, with coefficients related by  $\mathcal{R}$ . We seek a self-consistent solution of the ZZ equations based on this assumption.

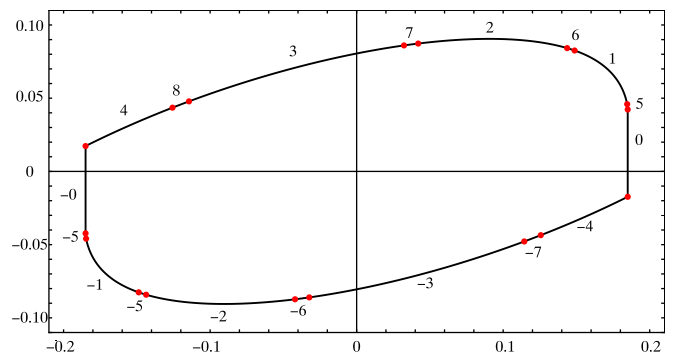


FIG. 17. Plot of the attractor for  $\tau = 35$ ,  $d = 0.63$ , with segments  $\xi_j$  labeled  $\pm 0, \pm 1, \dots, \pm 8$ . With decreasing  $d$ , the segments 5,6,7,8 shrink, vanishing at  $d = d_* = 0.6135 \dots$

Further assumptions are continuity, which implies the relations

$$x_5(0) = x_0(l), \quad x_1(0) = x_5(\delta_1), \quad x_6(0) = x_1(l), \quad \text{etc.},$$

and inversion symmetry of the periodic orbit. The latter requires that the return flight, from  $x = -L$  to  $x = L$ , is just the inverted image of the outgoing flight, with a corresponding decomposition into time intervals  $S_{-n}$ , with basis-function coefficients equal to the negatives of their outgoing counterparts.

The above prescription does not yet pin down a complete solution to the ZZ equations. In particular, we need to link segments  $S_4$  and  $S_5$ , coordinate the set of interlocking continuity relations, and, finally, bring into play the locked motion which connects the outgoing and return flights at both ends. The fact that  $S_4$  is of length  $\delta_2 < l$  is not a problem, the coefficients of  $x_4(s), y_4(s)$  are still obtained from those of  $x_3(s), y_3(s)$  via  $\mathcal{R}$ . However, solving the DDE for  $S_5$  requires knowledge of  $x(t)$  in an interval of length  $\delta_1$  contained in  $S_{-4}$  of length  $\delta_2 > \delta_1$ . Thus, before applying  $\mathcal{R}$ , we must shift the origin of the local time variable by  $\delta_2 - \delta_1$ .

Let us denote by  $(\hat{X}_n, \hat{Y}_n)$  the upper endpoints of orbit segments  $\xi_n$ ,  $n = 0, 1, \dots, 8$ . We fix  $\delta_1, \delta_2$ , and  $l = \tau - \delta_1$ , as well as

$$\hat{X}_0 = L, \quad \hat{X}_4 = -L,$$

and solve Eqs. (1) for the initial locking interval,

$$\xi_0(s) = (L, L - (L + \hat{Y}_4)e^{-cs}). \quad (24)$$

We then calculate, in order, all  $\xi_n$  as linear functions of the unknown  $(\hat{X}_n, \hat{Y}_n)$ :

$$\xi_j = \mathcal{R}(\xi_{j-1}, (\hat{X}_{j+5}, \hat{Y}_{j+5})), \quad j = 1, 2, 3, 4,$$

$$\xi_5 = \mathcal{R}(T_{\delta_2 - \delta_1}(-\xi_4), (\hat{X}_0, \hat{Y}_0)),$$

$$\xi_j = \mathcal{R}(\xi_{j-1}, (\hat{X}_{j-5}, \hat{Y}_{j-5})), \quad j = 6, 7, 8,$$

where the translation operator  $T_{\Delta s}$  performs the substitution  $s \rightarrow s + \Delta s$ .

Defining the length of interval  $S_n$  as

$$w_n = \begin{cases} l & n \leq 3, \\ \delta_1 & 5 \leq n \leq 8, \\ \delta_2 & n = 4, \end{cases}$$

we find that the 16 equations,

$$x_n(w_n) = \hat{X}_n, \quad y_n(w_n) = \hat{Y}_n, \quad n = 1, \dots, 8,$$

provide a 16-dimensional matrix equation for the unknown  $\hat{X}_n$  and  $\hat{Y}_n$ . Note that this list includes  $\hat{Y}_0$ , but not  $\hat{X}_4$ . If the matrix relation is nonsingular, which we must verify for our given  $\delta_1, \delta_2$ , we can solve for all segment endpoints. Plugging back into the recursion relations gives numerical values for all the basis-function coefficients. To calculate  $\delta_1$  and  $\delta_2$ , we need to solve two additional equations,

$$\epsilon_1(\delta_1, \delta_2) = y_0(l) = L - (L + \hat{Y}_4)e^{-cl} - \hat{Y}_0 = 0,$$

$$\epsilon_2(\delta_1, \delta_2) = \dot{x}_5(0) = a(L - \hat{Y}_0) + b x_4(\delta_2 - \delta_1) = 0.$$

The first of these applies Eq. (24) to connect the initial point,  $(L, -\hat{Y}_4)$ , on the locked interval to the final point,  $(L, \hat{Y}_0)$ . The second equation uses the first equation of Eqs. (1) to set  $\dot{x}$  to zero at the moment of unlocking. Together these

equations allow us to determine uniquely the values of  $\delta_1$  and  $\delta_2$ , hence  $l = \tau - \delta_1$ , and thereby complete the self-consistent construction of the periodic attractor.

We carried out the above scheme for  $d = 0.63$  using Mathematica® to implement the eight successive recursion operations and to solve the matrix equation for the segment endpoints. This allowed us to calculate  $\epsilon_1$  and  $\epsilon_2$  for any given input  $\delta_1$  and  $\delta_2$ . We then systematically reduced the error function  $\sqrt{\epsilon_1^2 + \epsilon_2^2}$  by making small changes in  $\delta_1$  and  $\delta_2$ . Using 16-digit precision, we obtained 7-digit values for  $\delta_1$  and  $\delta_2$ , while for 40- and 100-digit precision, we obtained values correct to 27 and 51 digits, respectively,

$$\delta_1 = 2.41266836668223750021815303199\dots,$$

$$\delta_2 = 13.1251394179853464079249424144\dots$$

We then computed all of the basis-function expressions for the orbit, plotted in Fig. 17.

## VI. PERIODIC ORBIT CONSTRUCTION FOR ALL $d$ AND $\tau$

Our numerical explorations of Sec. II give strong evidence for the existence of a nontrivial periodic attractor for each possible plate length  $d$  and delay time  $\tau$  in regions Ia and Ib of the phase diagram. For Ia, and on the boundary curve  $\mathcal{C}'$ , the locking time  $l$  is at least as long as the delay time  $\tau$ , the outgoing flight is a chain of time intervals  $S_n$  of length  $\delta_1 = \tau$ , plus one of length  $\delta_2 < \delta_1$  if the flight time is not a multiple of  $\tau$ . The orbit on each  $S_n$  is a basis function  $\xi_n$  of degree  $n$ , related to that on  $S_{n-1}$  by the recursion operation  $\mathcal{R}$ .

For Ib, with  $l < \tau$ , the situation is more complicated, as we confirmed for  $\tau = 35, d = 0.63$  (see Fig. 17). For that case, the temporal order of intervals  $S_n$  of lengths  $l, \delta_1$ , and  $\delta_2$  on the outgoing flight was easy to guess, specified by the *itinerary*

$$(0, 5, 1, 6, 2, 7, 3, 8, 4).$$

By assuming inversion symmetry and a basis-function form, we were able, for given interval lengths  $\delta_1$  and  $\delta_2$ , to determine all coefficients using the recursion operation  $\mathcal{R}$ . Precise values of  $\delta_1$  and  $\delta_2$  were then obtained by solving simultaneously the  $\dot{y}$  equation for locked phases and the unlocking condition  $\dot{x} = 0$ .

We can follow the same pattern generally on Ib, starting with a systematic determination of the itinerary. We shall see that the itinerary lengths increase without bound as one approaches the critical line, with  $l$  tending to zero. A similar phenomenon will be seen to occur as one approaches a “resonant” case where the half-period  $r$  and delay time  $\tau$  are rationally related.

### A. Construction of the attractor

Let us now go through our procedure for constructing the complete periodic attractor for all nonresonant subcritical  $\tau$  and  $d$  values. In following the details, the reader may find helpful the illustrative example of Appendix B.

We begin with a Runge-Kutta simulation which we need to obtain reliable values of the flight and locking times, good enough to produce the relevant itinerary  $\iota$  with a high degree of certainty. An efficient algorithm for extracting the itinerary is presented in Appendix A.

Having calculated the itinerary, we then seek a solution of the DDE on the outgoing flight portion of the orbit, as a precise function of  $\delta_1$  and  $\delta_2$ . We begin by treating the upper endpoints  $(\hat{X}_n, \hat{Y}_n)$  of the  $N + 1$  segments  $\xi_0, \xi_1, \dots, \xi_N$  as unknowns, with the exception of  $\hat{X}_0 = L$  and  $\hat{X}_{i(N)} = -L$ . We then construct, for  $n = 1, \dots, N$ , the basis-function  $\xi_n(s)$  by applying the  $\mathcal{R}$  function on  $\pm \xi_{n-1}(s)$ , with the minus sign for  $t_n < \tau$ . The segment  $\xi_{i(1)}$  requires an additional origin shift, since its partner segment under inversion results from the truncation of the  $\tau$  translate of  $\xi_{i(1)-1}$ . This is taken care of by replacing  $s$  by  $s + \sigma$  in the expression for  $-\xi_{i(1)-1}$ , before applying  $\mathcal{R}$ , with  $\sigma = \delta_2 - \delta_1$  if  $i(N) < i(1)$  and  $\sigma = l - \delta_1$  otherwise. The resulting  $\xi_n(s)$  depend linearly on the  $2N$  unknown endpoint coordinates. By setting

$$\xi_n(w_n(\delta_1, \delta_2)) = (\hat{X}_n, \hat{Y}_n), \quad n = 1, \dots, N,$$

we obtain a  $2N$ -dimensional matrix equation for the endpoint coordinates.

As in the example of Sec. V, the final stage in the construction is to pin down the values of  $\delta_1$  and  $\delta_2$  through numerical solution of the simultaneous equations

$$L - (L + \hat{Y}_{i(N)})e^{-cl} - \hat{Y}_0 = 0, \quad a(L - \hat{Y}_0) + b x_{i(1)-1}(\sigma) = 0, \quad (25)$$

with  $\sigma = \delta_2 - \delta_1$  if  $i(N) < i(1)$  and  $\sigma = l - \delta_1$  otherwise. With  $\delta_1$  and  $\delta_2$  in hand, we can complete the calculation all  $\hat{X}_j, \hat{Y}_j$  and  $\xi_j(s)$ ,  $j = 0, \dots, N$ .

### B. Sequence of itineraries for $\tau = 35$

We now survey the sequence of itineraries encountered as one continuously increases  $d$  from  $d_*$  to its critical value with the delay time  $\tau$  held fixed at 35. Over the interval  $d_* = 0.613527 \dots \leq d \leq 0.764595 \dots$ , we performed over 80 fourth-order Runge-Kutta simulations of the ZZ equations, using a time step  $\Delta t = 0.01 = \tau/3500$  to extract accurate values of the per-cycle flight time  $f$ , locking time  $l$ , and half-period  $r = l + f$  on the attractor. Floating-point error was avoided by using 100-digit precision and in each case enough iterations were executed to ensure convergence to a periodic attractor.

For  $d$  values approaching  $d_{\text{crit}}$ , the Runge-Kutta simulations become excessively time-consuming. At that point we make use of extrapolation to obtain values of  $f$ ,  $l$ , and  $r$ . We find empirically that for  $0.764 < d \leq 0.764595$ , the Runge-Kutta based values of  $r$  can be accurately approximated by a fourth-degree polynomial in  $d - d_{\text{crit}}$ , while those for  $f$  and  $l$  are well fit by fourth-degree polynomials in  $(d - d_{\text{crit}})^{1/2}$ . Specifically, with  $\hat{d} = d_{\text{crit}} - d \leq 0.0006$ ,  $d_{\text{crit}} = 0.7645997799038989$ , and  $r_{\text{crit}} = f_{\text{crit}} = 127.43079937722544$ ,

$$\begin{aligned} r - r_{\text{crit}} &= 50.338381124842314 \hat{d} + 28989.66960524308 \hat{d}^2 \\ &\quad - 3.6287890695628986 \times 10^7 \hat{d}^3 \\ &\quad + 2.239854160114137 \times 10^{10} \hat{d}^4, \\ f - f_{\text{crit}} &= -94.12242121842485 \sqrt{\hat{d}} + 168.47472707701996 \hat{d} \\ &\quad - 47.82488059320736 \hat{d}^{3/2} + 24.315355198260377 \hat{d}^2, \end{aligned}$$

$$\begin{aligned} l &= 94.12220602939439 \sqrt{\hat{d}} - 120.30313203961904 \hat{d} \\ &\quad + 544.8441322617502 \hat{d}^{3/2} - 1416.6075307376366 \hat{d}^2. \end{aligned}$$

Using the Runge-Kutta values for  $d \leq 0.764595$  and the extrapolated results for  $0.764595 < d < d_{\text{crit}}$ , we have used the algorithm of Appendix A to calculate the itineraries up to  $d = 0.76459977902$ , within  $10^{-9}$  of the critical value. Over that range, the locking time decreases monotonically, while the flight time (respectively, cycle period) increases (respectively, decreases) monotonically. The  $d$  intervals of constant itinerary are conveniently grouped into families, on each of which the half-period  $r$  decomposes as

$$r = r_0 l + (r_1 + n r_0) \delta_1 + r_0 \delta_2 \quad (26)$$

or

$$r = r_0 l + r_0 \delta_1 + (r_2 + n r_0) \delta_2, \quad (27)$$

where  $n$  ranges over a finite or infinite sequence of nonnegative integers. Each family is bounded by special  $d$  values which we call *resonances* and *cross-overs*. At a cross-over, either  $\delta_1$  or  $\delta_2$ , having tended to  $l$  from below, discontinuously drops to zero. The itinerary of the cross-over point is well defined, namely that of the successor family. At a resonance, there is a rational relation between  $r$  and  $\tau$ , with  $\delta_1 = \delta_2 = 0$ . At such a point, the orbit cannot be assigned an itinerary, not even a countably infinite one. Only the  $\tau$ -translates of the boundary interval of length  $l$  are basis functions, and these alternate with non-basis-function pieces of the orbit. The results of our calculations are displayed in Table I.

An interesting feature of the itinerary families is the extent to which the content of Table I is constrained by number-theoretic considerations. This is most obvious in the case of resonances, where there is a rational relation between the two main time scales of the attractor, the cycle half-period  $r$  and the delay time  $\tau$ . The possibly resonant values of  $r/\tau$  can be read off from the list of continued-fraction approximants to the *critical* ratio  $r_{\text{crit}}/\tau = 127.43079937722544/35$ , namely

$$\begin{aligned} &\frac{3}{1}, \frac{4}{1}, \frac{7}{2}, \frac{11}{3}, \frac{40}{11}, \frac{51}{14}, \frac{91}{25}, \frac{142}{39}, \frac{517}{142}, \frac{659}{181}, \frac{4471}{1228}, \\ &\frac{5130}{1409}, \frac{30121}{8273}, \frac{35251}{9682}, \frac{276878}{76047}, \dots \end{aligned}$$

Due to the monotonic decrease of  $r(d)$ , only those fractions greater than the critical ratio are available for the resonances, i.e.,  $4, 11/3, 51/14, 142/39, 659/181$ , etc. These numbers can easily be interpreted in terms of our “slider” model of Appendix A: an  $m/n$  resonance occurs if the slider arrives precisely at the target segment  $(f, r)$  in  $m$  steps of size  $\tau$ , having traversed  $n$  half-cycles of length  $r$ , provided that it has not overlapped the target interval previously. Looking at Table I, we see that resonances indeed occur for ratios  $4/1, 11/3, 659/181, 5130/1409, 35251/9682$ , but not for  $51/14$  and  $142/39$ , for which there are previous overlaps at 40 and 51 steps, respectively. We note also that the numerators of the rational approximants also play a role for the decompositions of  $r$  of the various families: the coefficient  $r_0$  is from that set, since it is equal to the number of steps required for the slider to overlap the target segment for the first time, a near-resonant event.

TABLE I. Itinerary families for  $\tau = 35$ .

$d$	Itinerary family
0.613527...	$d_*$ for $\tau = 35$ : $l = \tau, \delta_1 = 0$ $r = 4l + 4\delta_1 + (4n + 1)\delta_2,$ $\tau = l + \delta_1 + n\delta_2,$ $n = 0, 1, \dots,$
0.679683...	Resonance: $r = 4\tau, \delta_1 = \delta_2 = 0$ $r = 4l + (4n + 7)\delta_1 + 4\delta_2,$ $\tau = l + (n + 2)\delta_1 + \delta_2,$ $n = \dots, 1, 0.$
0.748004...	Cross-over: $\delta_1 = 0$ $r = 11l + 11\delta_1 + (11n + 4)\delta_2,$ $\tau = 3l + 3\delta_1 + (3n + 1)\delta_2,$ $n = 0, 1, \dots$
0.75424...	Resonance: $3r = 11\tau, \delta_1 = \delta_2 = 0$ $r = 11l + (11n + 29)\delta_1 + 11\delta_2,$ $\tau = 3l + (3n + 8)\delta_1 + 3\delta_2,$ $n = \dots, 1, 0$
0.763809...	Cross-over: $\delta_1 = 0$ $r = 40l + 40\delta_1 + 11\delta_2,$ $\tau = 11l + 11\delta_1 + 3\delta_2$
0.764091...	Cross-over: $\delta_2 = 0$ $r = 51l + 40\delta_1 + 51\delta_2,$ $\tau = 14l + 11\delta_1 + 14\delta_2$
0.764507...	Cross-over: $\delta_1 = 0$ $r = 91l + 91\delta_1 + 51\delta_2,$ $\tau = 25l + 25\delta_1 + 14\delta_2$
0.764508...	Cross-over: $\delta_2 = 0$ $r = 142l + (142n + 91)\delta_1 + 142\delta_2,$ $\tau = 39l + (39n + 25)\delta_1 + 39\delta_2,$ $n = 0, 1, 2, 3$
0.764595...	Cross-over: $\delta_1 = 0$ $r = 659l + 659\delta_1 + (659n + 142)\delta_2,$ $\tau = 181l + 181\delta_1 + (181n + 39)\delta_2,$ $n = 0, 1, \dots$
0.76459700...	Resonance: $181r = 659\tau, \delta_1 = \delta_2 = 0$ $r = 659l + (659n + 3812)\delta_1 + 659\delta_2,$ $\tau = 181l + (181n + 1047)\delta_1 + 181\delta_2,$ $n = \dots, 1, 0, 1$
0.764599711...	Cross-over: $\delta_1 = 0$ $r = 5130(l + \delta_1) + (5130n + 659)\delta_2,$ $\tau = 1409(l + \delta_1) + (1409n + 181)\delta_2,$ $n = 0, 1, \dots$
0.7645997280...	Resonance: $1409r = 5130\tau, \delta_1 = \delta_2 = 0$ $r = 5130(l + \delta_2) + (5130n + 24991)\delta_1,$ $\tau = 1409(l + \delta_2) + (1409n + 6864)\delta_1,$ $n = \dots, 1, 0, 1$
0.7645997284...	Cross-over: $\delta_1 = 0$ $r = 35251(l + \delta_1) + (35251n + 5130)\delta_2,$ $\tau = 9682(l + \delta_1) + (9682n + 1409)\delta_2,$ $n = 0, 1, \dots$
0.76459977902...	Resonance: $9682r = 35251\tau, \delta_1 = \delta_2 = 0$

**C. Application to  $\tau = 10$**

The value  $\tau = 35$  was chosen for illustrative purposes, making possible explicit high-precision constructions of the subcritical periodic attractors as well as a detailed account of

TABLE II. Near-critical values of  $d, l,$  and  $r$  for  $\tau = 10$ .

$d$	$l$	$r$
0.57605	1.2574117154	214.1816426056
0.576055	1.0971675561	214.1820799154
0.57606	0.9082388155	214.1825300724
0.5760625	0.7967248754	214.1827607752
0.576065	0.6664084711	214.1829959212
0.5760707834	0	214.1835645497

the piecewise analytic behavior as one approaches the critical curve in parameter space. Now we want to apply what we have learned to a delay time encountered in the actual ZZ experiments, namely  $\tau = 10$ . As before, we carry out a number of modified Runge-Kutta simulations, with five-point interpolation employed to capture accurately the contacts with the boundaries at  $x = \pm L$ . These give us, for each  $d$ , reliable values for the locking time  $l$  and half-period  $r$ , with the flight time  $f$  given by  $r - l$ . We display the  $d, l,$  and  $r$  values, rounded to 10-digit accuracy (comparable to the truncation accuracy of the numerical integration), in Table II.

This information is fed into our auxiliary “slider” model of Appendix A to calculate the itinerary patterns. The Runge-Kutta simulations become increasingly time-consuming as we approach the critical value of  $d$ , and so we fit our data with low-degree polynomials in  $\hat{d} = d - d_{\text{crit}}$  for  $r$  and in  $\hat{d}^{1/2}$  for  $l$  and  $f$ . In the  $\tau = 35$  example, this worked well, and it turns out to be at least as effective for  $\tau = 10$  in exploring the near-critical regime. Specifically, using  $l$  as our independent variable, tending to zero at criticality,

$$r(l) = 214.1835645496504767 - 0.0012991199446723 l + 0.0000532869912895 l^2,$$

$$d(l) = 0.5760707834045230 - 0.0000129857320455 l^2 - 1.0095082304893257 \times 10^{-7} l^4.$$

The function  $r(l) - r_{\text{crit}}$ , fitting the values of Table II, is shown in Fig. 18.

The successive itinerary families for  $d_* < d < d_{\text{crit}}$  are shown in Table III. The last entry corresponds to

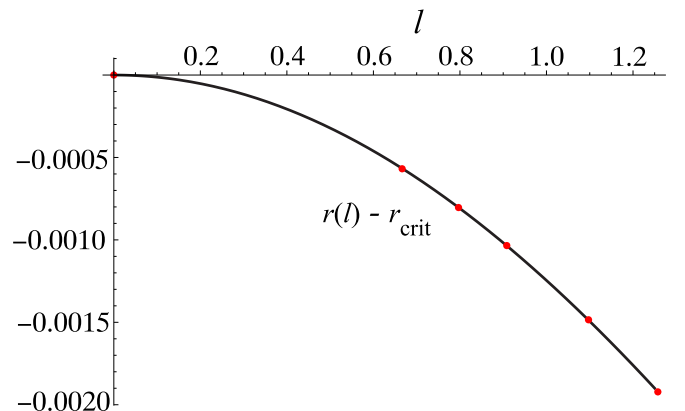


FIG. 18. The function  $r(l) - r_{\text{crit}}$  with the points of Table II shown as red dots.

$d_{\text{crit}} - d(10^{-5}) = O(10^{-15})$ . As explained in Appendix A, the family itineraries can easily be extracted from the listed decompositions of  $r$  and  $\tau$ .

The pattern once again reflects the sequence of continued-fraction convergents of the critical  $r/\tau$  ratio, namely

$$21, \frac{43}{2}, \frac{107}{5}, \frac{150}{7}, \frac{257}{12}, \frac{921}{43}, \frac{1178}{55}, \frac{2099}{98}, \frac{17970}{839}, \frac{20069}{937}, \frac{12601233}{588338},$$

$$\frac{12621302}{589275}, \frac{37843837}{1766888}, \frac{50465139}{2356163}, \frac{88308976}{4123051}, \frac{138774115}{6479214}, \frac{227083091}{10602265}, \dots$$

Possible resonant values are the alternating convergents  $21, \frac{107}{5}, \frac{257}{12}, \dots$ , none of which is realized in Table III, in striking contrast to the  $\tau = 35$  example. There is, however, an interesting new feature. The convergent  $20069/937$  is remarkably close to the critical value, so close that the numerator of the next convergent is over 600 times 20069. This reflects the appearance in the continued fraction expansion of an unusually large denominator,

$$\frac{12601233}{588338} = 21 + \frac{1}{2 + \frac{1}{1 + \frac{1}{2 + \frac{1}{1 + \frac{1}{3 + \frac{1}{1 + \frac{1}{1 + \frac{1}{8 + \frac{1}{1 + \frac{1}{627}}}}}}}}}}}$$

As one decreases  $l$  from 0.0105 to .000017, almost three orders of magnitude, the size of the intervals  $\delta_i$  decreases steadily, just as one might expect for a resonance. The latter is not possible, of course, since  $20069/937$  is slightly greater than the critical ratio. We have verified that the family terminates at  $n = 627$ , and have found a member of the next family, listed at the end of Table III.

**VII. CONCLUSIONS**

The model used by Zhong and Zhang [4] to successfully describe the motion of an insulating plate on the surface of a convecting fluid turns out to be an interesting dynamical system in its own right.

As shown in Ref. [4] and revisited in Sec. II above, the system obeys linear differential equations with delay time  $\tau$  for the plate length larger than a critical value  $d_{\text{crit}}$ . These equations can be solved analytically, providing an accurate phase diagram in the  $d, \tau$  plane and a relatively simple description of the approach to  $d_{\text{crit}}$  from above.

In contrast, the subcritical behavior is far from simple. Given unavoidable locking at the boundaries, the system is nonlinear, with orbits which are piecewise analytic. From high-precision numerical integration we have verified empirically that the orbit, for a given  $d \leq d_{\text{crit}}$  tends asymptotically to a periodic orbit which alternates between locked and unlocked motions. For  $d$  approaching criticality, the locking phase shortens, and convergence to the periodic attractor is nontrivial, requiring good control over both the time increment  $\Delta t$  and the overall time  $t$  of the numerical integration.

TABLE III. Itinerary families for  $\tau = 10$ .

---



---

$r = 21l + 21\delta_1 + (1 + 21n)\delta_2,$	$\tau = l + \delta_1 + (0 + n)\delta_2, \quad n = 0, 1,$
$r = 43l + (21 + 43n)\delta_1 + 43\delta_2,$	$\tau = 2l + (1 + 2n)\delta_1 + 2\delta_2, \quad n = 0, 1,$
$r = 107l + 107\delta_1 + 43\delta_2,$	$\tau = 5l + 5\delta_1 + 2\delta_2,$
$r = 150l + 107\delta_1 + 150\delta_2,$	$\tau = 7l + 5\delta_1 + 7\delta_2,$
$r = 257l + 257\delta_1 + (150 + 257n)\delta_2,$	$\tau = 12l + 12\delta_1 + (7 + 12n)\delta_2, \quad n = 0, 1, 2,$
$r = 921l + 257\delta_1 + 921\delta_2,$	$\tau = 43l + 12\delta_1 + 43\delta_2,$
$r = 1178l + 1178\delta_1 + 921\delta_2,$	$\tau = 55l + 55\delta_1 + 43\delta_2,$
$r = 2099l + (1178 + 2099n)\delta_1 + 2099\delta_2,$	$\tau = 98l + (55 + 98n)\delta_1 + 98\delta_2, \quad n = 0, 1, \dots, 7,$
$r = 17970l + 17970\delta_1 + 2099\delta_2,$	$\tau = 839l + 839\delta_1 + 98\delta_2,$
$r = 20069l + (17970 + 20069n)\delta_1 + 20069\delta_2,$	$\tau = 937l + (839 + 937n)\delta_1 + 937\delta_2, \quad n = 0, 1, \dots, 627,$
$r = 12621302l + 12601233\delta_1 + 12621302\delta_2,$	$\tau = 589275l + 588338\delta_1 + 589275\delta_2$

---



---

Fortunately, the subcritical orbits can be determined analytically, making use of the computational algebra and arbitrary precision arithmetic available with Mathematica. The algorithm was derived in Secs. IV–VI above, with applications to the values  $\tau = 35$  and  $\tau = 10$ . Each orbit is inversion symmetric and has two locking intervals alternating with two flights. Each flight consists of  $n$  segments, with each segment a linear combination of terms of the form  $(t - t_0)^k$

or  $(t - t_0)^k e^{(a-c)t}$ ,  $k = 0, \dots, k_{\max} \leq n$ . Recursion and continuity relations provide an algorithm for determining all the numerical coefficients with arbitrary precision.

A combination of numerical and analytical results allowed us to obtain empirical power-series for the the flight and locking intervals as  $d$  approaches  $d_{\text{crit}}$ . A rigorous mathematical derivation of these results is lacking at the present time. If future investigations can establish these formulas, our analysis shows how a rigorous description of the evolution of the piecewise analytic structure of the orbits would follow.

It is interesting to compare the near-critical behavior of the deterministic ZZ model with that of the same model with noise added. We deal with this in Appendix C.

## ACKNOWLEDGMENTS

The author thanks Jun Zhang, Jin-Qiang Zhong, Jinzi Mac Huang, and Laurent Mertz for helpful discussions. Remarks and recommendations of a referee were valuable in arriving at the final version of the article.

## APPENDIX A: ALGORITHM FOR DETERMINING ITINERARIES

For given  $\tau$  and  $d_* \leq d < d_{\text{crit}}$ , we can easily determine the itinerary using the following algorithm, provided we have in hand (e.g., from a numerical simulation) accurate values of the locking time  $l$  and flight time  $f$ . Consider a reentrant line segment  $\mathcal{L} = \{t : 0 \leq t \leq r = f + l\}$  with a 1D slider of length  $w$  initially having  $w = l$ . We translate the slider along the  $t$  axis in steps of length  $\tau$  modulo  $r$ . At the  $n$ th step, the slider covers a half-open interval  $S_n$  of length  $w_n$  and leading endpoint  $t_n$ . If the slider overlaps the interval  $(f, r)$ , the overlap portion is “eaten” and the remaining piece proceeds forward. Eventually, the truncated slider enters  $(f, r)$  fully and the process halts. At that point, the reentrant time axis  $\mathcal{L}$  has been completely covered by the intervals  $S_n$  and their temporal order is the itinerary. A precise statement of the algorithm is the following:

- (1) Step 0:  $t_0 = 0$ ,  $w_0 = l$ .
- (2) Step  $n$ :
  - (i) If  $t_n + \tau \leq f$ , set  $t_{n+1} = t_n + \tau$ ,  $w_{n+1} = w_n$ .
  - (ii) If  $t_n + \tau \geq r + w_n$ , set  $t_{n+1} = t_n + \tau - r$ ,  $w_{n+1} = w_n$ .
  - (iii) If  $r < t_n + \tau < r + w_n$ , set  $t_{n+1} = w_{n+1} = \delta_1 = t_n + \tau - r$ .
  - (iv) If  $f < t_n + \tau < f + w_n$ , set  $t_{n+1} = f$ ,  $w_{n+1} = \delta_2 = f - t_n - \tau + w_n$ .
  - (v) If  $f + w_n \leq t_n + \tau \leq r$ , record  $N = n$  and halt.
- (3) Output the sequences of  $w_n$  and  $t_n$ , as well as the itinerary, the permutation  $\iota$  of  $\{0, 1, \dots, N\}$  such that  $t_{\iota(n+1)} = t_{\iota(n)} + w_{n+1}$ .

It is not difficult to prove that the closed intervals of length  $w_1, \dots, w_N$  completely cover the flight, sharing only their mutual endpoints. Moreover, there are only two truncation events, producing intervals of lengths  $\delta_1$  and  $\delta_2$  at positions 1 and  $N$  of the itinerary, respectively. These events can occur in either order.

The identities

$$r = \sum_{n=0}^N w_n, \quad \tau = t_1 = \sum_{k=1}^M w_{\iota(k)}, \quad M = \iota^{-1}(1), \quad (\text{A1})$$

allow us to decompose  $f$ ,  $r$ , and  $\tau$  as integer linear combinations of  $l$ ,  $\delta_1$ , and  $\delta_2$ . The itinerary can be recovered from a knowledge of  $N$  and  $M$  alone:

$$\iota^{-1}(k) = kM \bmod (N + 1).$$

## APPENDIX B: EXAMPLE OF ORBIT CONSTRUCTION FOR REGION I<sub>b</sub>

In this Appendix we illustrate the attractor orbit construction with a step-by-step description of the case  $\tau = 35$ ,  $d = 0.7$ .

### 1. Numerical integration of the ZZ equations

The first stage of the construction is a numerical integration of the ZZ equations of motion using the modified Runge-Kutta scheme of Sec. II, with 100-digit working precision, time step 0.01s, and a total time of  $2000\tau = 70000$ . By the end, the orbit has converged to a periodic attractor, an approximation to the exact attractor we hope to construct, with values for the locking time  $l$ , flight time  $f$  and half-period  $r$

$$l = 21.5620605711388, \quad f = 114.504570386893, \quad (\text{B1})$$

$$r = 136.066630958031. \quad (\text{B2})$$

### 2. Partition of the time axis

Using the numerically generated values of  $l$ ,  $f$ , and  $r$ , the “slider” algorithm of Appendix A generates the partition of the time axis displayed in Fig. 19, with the itinerary and its inverse,

$$\iota = (0, 4, 8, 12, 16, 1, 5, 9, 13, 17, 2, 6, 10, 14, 18, 3, 7, 11, 15),$$

$$\iota^{-1} = (0, 5, 10, 15, 1, 6, 11, 16, 2, 7, 12, 17, 3, 8, 13, 18, 4, 9, 14),$$

and constitutive relations

$$r = f + l = 4l + 11\delta_1 + 4\delta_2, \quad \tau = l + 3\delta_1 + \delta_2. \quad (\text{B3})$$

From the numerical integration and partition of the time axis, we can now display, in Fig. 20, the attractor partitioned into 38 segments

$$\xi_{\pm j}(s) = (x_{\pm j}j(s), y_{\pm j}(s)), \quad 0 \leq s \leq w_j, \quad j = 0, \dots, 18.$$

### 3. Recursive solution

Our recursion begins with formulas for the locked portions of the orbit,

$$\xi_{\pm 0}(s) = \pm(L, L - (L + \hat{Y}_{15})e^{-cs}).$$

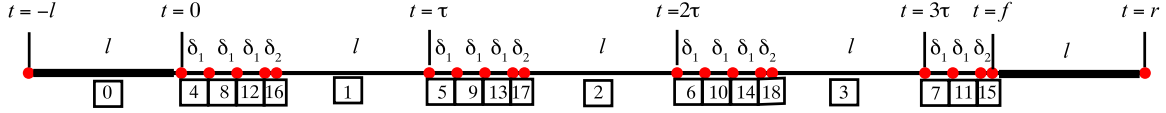


FIG. 19. Partition of the time axis into intervals  $S_n$  of length  $w_n \in \{l, \delta_1, \delta_2\}$ . In the figure,  $S_n$  is represented by its integer subscript, boxed, placed below the time axis, with the width  $w_n$  placed directly above. Also noted are the event times  $t = 0$  (flight launch),  $\tau, 2\tau, 3\tau, f$  (flight arrival), and  $r$  (half-period). The order and widths of the segments are determined by the slider model of Appendix A.

Recall that the arrival point of the incoming flight is  $(-\hat{X}_{15}, -\hat{Y}_{15})$ , where  $\hat{X}_{15} = -L$  and  $\hat{Y}_{15} = y_{15}(w_{15})$ . The latter quantity is unevaluated at this stage.

The remaining orbit segments are obtained by sequential application of the operator  $\mathcal{R}$  of Eq. (20), embodying the sequence of linear updates in Eqs. (7)–(19). In particular, defining the predecessor function

$$\pi(j) \stackrel{\text{def}}{=} \iota(\iota^{-1} - 1),$$

we have

$$\begin{aligned} \xi_j &= \mathcal{R}(\xi_{j-1}, (\hat{X}_{\pi(j)}, \hat{Y}_{\pi(j)})), & j = 1, 2, 3, \\ \xi_4 &= \mathcal{R}(T_{l-\delta_1}(-\xi_3), (\hat{X}_{\pi(4)}, \hat{Y}_{\pi(4)})), \\ \xi_j &= \mathcal{R}(\xi_{j-1}, (\hat{X}_{\pi(j)}, \hat{Y}_{\pi(j)})), & j = 5, 6, 7, \\ \xi_8 &= \mathcal{R}(-\xi_7, (\hat{X}_{\pi(8)}, \hat{Y}_{\pi(8)})), \\ \xi_j &= \mathcal{R}(\xi_{j-1}, (\hat{X}_{\pi(j)}, \hat{Y}_{\pi(j)})), & j = 9, 10, 11, \\ \xi_{12} &= \mathcal{R}(-\xi_{11}, (\hat{X}_{\pi(12)}, \hat{Y}_{\pi(12)})), \\ \xi_j &= \mathcal{R}(\xi_{j-1}, (\hat{X}_{\pi(j)}, \hat{Y}_{\pi(j)})), & j = 13, 14, 15, \\ \xi_{16} &= \mathcal{R}(-\xi_{15}, (\hat{X}_{\pi(16)}, \hat{Y}_{\pi(16)})), \\ \xi_j &= \mathcal{R}(\xi_{j-1}, (\hat{X}_{\pi(j)}, \hat{Y}_{\pi(j)})), & j = 17, 18. \end{aligned}$$

Note the shortening and origin shift of segment  $-\xi_3$  prior to application of  $\mathcal{R}$  to obtain  $\xi_4$ . The recursive construction outputs each  $\xi_j$ ,  $j = 1, \dots, 18$  as a basis function of degree  $j$ , i.e.,

$$\begin{aligned} x_j(s) &= \sum_{k=0}^j s^k (x_{j,k} + x_{j,k}^e e^{\alpha s}), & x_{j,j}^e &= 0, \\ y_j(s) &= \sum_{k=0}^j s^k (y_{j,k} + y_{j,k}^e e^{\alpha s}), & y_{j,j}^e &= 0, \end{aligned}$$

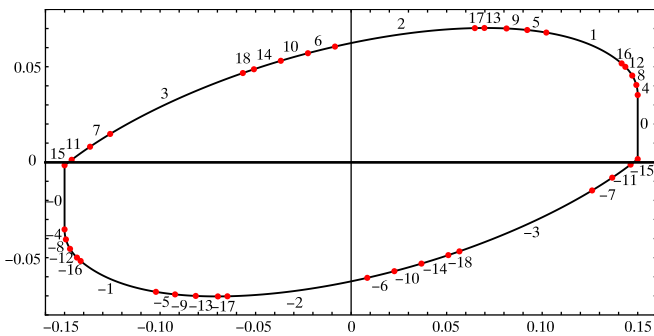


FIG. 20. Partition of the attractor into 38 segments  $\xi_{\pm j}$ , labeled by their respective subscripts. The endpoints  $(\hat{X}_j, \hat{Y}_j)$  are indicated by red dots. Time  $t = 0$  corresponds to the upper endpoint of  $\xi_0$ .

where  $x_{j,k}, x_{j,k}^e, y_{j,k}, y_{j,k}^e$  are linear in  $\hat{X}_k, \hat{Y}_k$ ,  $k = 0, \dots, 18$  and, for  $j \geq 4$ , can depend on  $\delta_1$  and  $\delta_2$ . For example, rounding off the floating-point numbers to six digits,

$$\begin{aligned} x_{4,1}^e &= e^{-4\alpha\delta_1 - \alpha\delta_2} \{ -9.76792 + 15.3608 \hat{X}_{16} \\ &+ 1.13137 \hat{X}_{17} + 0.153779 \hat{X}_{18} + \delta_1^2 [-0.00100012 \\ &+ 0.00288923 (\hat{X}_{16} - \hat{Y}_{16})] + \delta_2^2 [-0.0000625074 \\ &+ 0.000180577 (\hat{X}_{16} - \hat{Y}_{16})] - 19.8615 \hat{Y}_{16} \\ &+ \delta_1 [-0.162006 + 0.309269 \hat{X}_{16} + 0.0298095 \hat{X}_{17} \\ &+ \delta_2 (-0.000500059 + 0.00144462 \hat{X}_{16} - 0.00144462 \hat{Y}_{16}) \\ &- 0.378061 \hat{Y}_{16} - 0.0298095 \hat{Y}_{17}] + \delta_2 (-0.0405016 \\ &+ 0.0773174 \hat{X}_{16} + 0.00745238 \hat{X}_{17} - 0.0945152 \hat{Y}_{16} \\ &- 0.00745238 \hat{Y}_{17}) - 1.48625 \hat{Y}_{17} - 0.153779 \hat{Y}_{18} \}. \end{aligned}$$

#### 4. Calculation of the segment endpoints

Setting

$$\hat{X}_0 = L, \quad \hat{X}_{15} = -L,$$

the segment endpoints  $\hat{X}_j$ ,  $j = 1, \dots, 17$ ,  $\hat{Y}_j$ ,  $j = 0, \dots, 18$  can now be calculated as functions of  $\delta_1$  and  $\delta_2$ , by solving the 36 simultaneous linear equations

$$\hat{X}_j = x_j(w_j), \quad \hat{Y}_j = y_j(w_j), \quad j = 1, \dots, 18.$$

Substituting into our expressions for  $x_j(s)$  and  $y_j(s)$  we can now construct the entire piecewise analytic orbit for any given  $\delta_1$  and  $\delta_2$ .

#### 5. Calculation of $\delta_1$ and $\delta_2$

The precise determination of  $\delta_1$  and  $\delta_2$  requires numerical solution of Eqs. (25), namely

$$\begin{aligned} \epsilon_1(\delta_1, \delta_2) &= L - (L + \hat{Y}_{15}) e^{-c(35 - 3\delta_1 - \delta_2)} - \hat{Y}_0 = 0, \\ \epsilon_2(\delta_1, \delta_2) &= a(L - \hat{Y}_0) + b x_3(35 - 4\delta_1 - \delta_2) = 0, \end{aligned}$$

with the appropriate substitutions for  $\hat{Y}_0, \hat{Y}_{15}$ , and  $x_3(s)$ . We obtained values of  $\delta_1$  and  $\delta_2$  with 46-digit precision, namely (with rounding)

$$\delta_1 = 3.933369038524113, \quad \delta_2 = 1.637832312159231,$$

so that

$$l = 35 - 3\delta_1 - \delta_2 = 21.56206057226843,$$

$$r = 4l + 11\delta_1 + 4\delta_2 = 136.0666309614759.$$

We note that the values of these quantities in Eqs. (B1) and (B2), obtained via our modified Runge-Kutta integration, agree with these values in their first 11 digits.

### 6. Complete solution

Substituting the self-consistent values of  $\delta_1$  and  $\delta_2$  back into our expressions for  $x_j(s)$  and  $y_j(s)$ ,  $j = \pm 0, \pm 1, \dots, \pm 18$ , we obtain a complete high-precision piecewise-analytic representation of the attracting orbit.

Throughout our self-consistent construction we have used 100-digit floating point arithmetic. We have checked that the already impressive precision of  $\delta_1$  and  $\delta_2$  applies to  $x_j(s)$  and  $y_j(s)$  as well.

### APPENDIX C: THE STOCHASTIC ZHONG-ZHANG MODEL

In this Appendix we consider a version of the Zhong-Zhang model in which the motion of the fluid upwelling is subjected to white noise [7]. We are especially interested in seeing how the near-critical behavior of the deterministic model is affected.

The  $x, y$  equations of motion become *stochastic delay differential equations* (SDDE) in each of the modes, locked and unlocked. When the plate is free of the boundaries,  $|x| < L$ , we have

$$\begin{aligned}\dot{x}(t) &= a[x(t) - y(t)] - b x(t - \tau), \\ \dot{y}(t) &= c[x(t) - y(t)] + \dot{w}_\sigma(t),\end{aligned}$$

where  $a(d)$ ,  $b(d)$ , and  $c(d)$  are the same as in the deterministic model, and  $w_\sigma$  is the Wiener process with standard deviation  $\sigma$ . When the plate is locked at one of the boundaries,  $x = \pm L$ , the equations reduce to

$$x(t) = \pm L, \quad \dot{y}(t) = c[\pm L - y(t)] + \dot{w}_\sigma(t).$$

When the plate, initially free, reaches the boundary  $x = \pm L$  from the left (respectively, right), it is locked in place until the quantity  $a(x(t) - y(t)) - b x(t - \tau)$  changes sign from positive to negative (respectively, negative to positive), at which point the unlocked motion resumes.

The plate length  $d$  is controlled by the experimenter, while the delay time  $\tau$  and noise factor  $\sigma$  are extracted by fitting the data. This differs from the assumptions of Ref. [7], where the simplifying assumptions  $\tau = 0$  and  $g = 0$  are made, and  $\sigma$  is assumed to be independent of  $d$ , taking the value 0.001 in metric units (0.00288842 in our preferred units where  $D = 1$ ) based on an experimental fit for  $d = 0.8$ .

The overall structure of our solution of the stochastic ZZ model equations is the same as for the deterministic version. First, we break up the integration range into intervals

$$I_n = [n\tau, (n+1)\tau], \quad n = -1, 0, 1, 2, \dots, N-1,$$

with each  $I_n$  subdivided into  $M$  time steps of duration  $\Delta t = \tau/M$ . The dynamical evolution is described as a random process (*Ito process*) linking  $x$  and  $y$  coordinates at time  $t + \Delta t$  to those at time  $t$  by means of a step accurate to order  $\Delta t^{3/2}$ . The method, devised by Kloeden, Platen, and Schurz [6] (see below for details), has been modified to accommodate a delay

term in the differential equation for  $x(t)$ . As in the deterministic case, we integrate the SDDE for each  $I_n$  in succession,  $n = 0, 1, 2, \dots, N-1$ , treating the  $x$  values of  $I_{n-1}$  as a forcing function. The values of  $x$  for all times of  $I_{-1}$ , together with the value of  $y$  at  $t = 0$ , are supplied as our initial condition. In our theoretical simulations, the initial condition is arbitrary, but its choice presumably will not affect long-time statistical results relevant to the experimental data.

For the numerical integration prescription of the unlocked motion, we adopt a relatively simple one with a moderate amount of accuracy, namely the (strong) order-3/2 method of Kloeden, Platen, and Schurz [6]. Suppose  $x_n$  and  $y_n$  are the  $x$  and  $y$  coordinates at time  $n\Delta t$ , where  $\Delta t = \tau/\nu$ ,  $\nu \in \mathbb{Z}$  is our chosen time increment. The  $x_n$  are specified for  $n = -\nu \dots, -1, 0$ , together with  $y_0$ . For  $n = 0, \dots, N$ , we introduce coefficients

$$a_1 = \frac{a(a-c)}{2}, \quad a_2 = \frac{ab}{6}, \quad c_1 = \frac{c(a-c)}{2}, \quad c_2 = \frac{cb}{6},$$

and calculate

$$\begin{aligned}x_{n+1} &= x_n + (a\Delta t + a_1\Delta t^2)(x_n - y_n) \\ &\quad - a_2(2x_{n+1-\nu} + x_{n-\nu})\Delta t^2 \\ &\quad - \frac{b}{2}(x_{n+1-\nu} + x_{n-\nu})\Delta t - a\Delta Z_n, \\ y_{n+1} &= y_n + (c\Delta t + c_1\Delta t^2)(x_n - y_n) \\ &\quad - c_2(2x_{n+1-\nu} + x_{n-\nu})\Delta t^2 - c\Delta Z_n + \Delta W_n,\end{aligned}$$

with

$$\Delta W_n = \Delta t^{1/2}r_1, \quad \Delta Z_n = \frac{1}{2}\Delta t^{3/2}\left(r_1 + \frac{1}{\sqrt{3}}r_2\right).$$

Random numbers  $r_1$  and  $r_2$  are, for each  $n$ , independently sampled from a normal distribution  $N(0, \sigma)$ . The terms involving the delayed coordinates  $x_{n-\nu}$  and  $x_{n+1-\nu}$  arise from integrals over  $x(t)$  using the trapezoidal approximations,

$$\begin{aligned}\int_{t_{n-\nu}}^{t_{n-\nu+1}} x(t) dt &\approx \left(\frac{x(t_{n-\nu}) + x(t_{n-\nu+1})}{2}\right)\Delta t, \\ \int_{t_{n-\nu}}^{t_{n-\nu+1}} \int_{t_{n-\nu}}^t x(s) ds dt &\approx \left(\frac{2x(t_{n-\nu+1}) + x(t_{n-\nu})}{6}\right)\Delta t^2.\end{aligned}$$

For the locked motion, we can use the same recursion formula for  $y_n$ , while holding  $x_n$  fixed at  $\pm L$ . The times of the locking and unlocking events are determined using a standard root-finding procedure (secant rule).

As in the deterministic case, it will be useful to explore the nature of the solutions for different parameter values. First, we fix  $\tau = 10$  and  $\sigma = 0.003$ , close to the empirical values assumed in Ref. [7], and vary  $d$  over the range 0.2–0.99. Plots of  $x(t)$  and  $y(t)$ , for  $390\,000 \leq t \leq 400\,000$  are shown in Fig. 21.

Far from the critical value  $d = 0.576\dots$  of the noise-free model with  $\tau = 10$ , and leaving aside for the moment the extreme values  $d \geq 0.9$ , the orbits are recognizable as noisy versions of the deterministic long-term attracting orbits. There is clearly a *subcritical zone* where the orbit, with probability near unity, visits the boundaries in alternating fashion, and a *supercritical zone* where the  $x$ -orbit is a kind of bounded

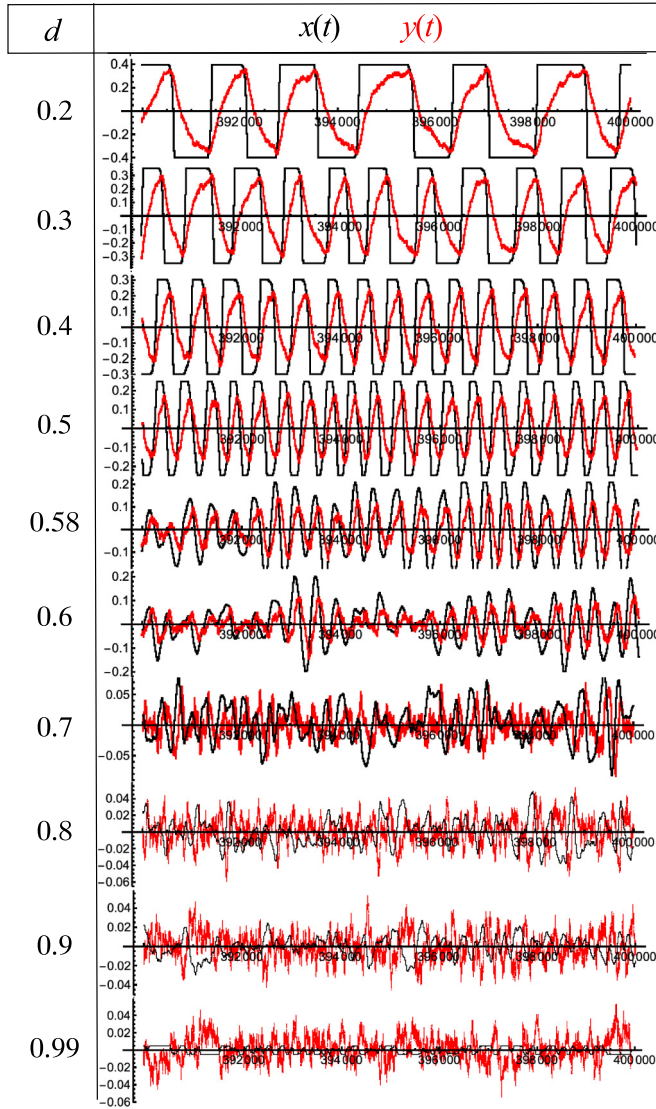


FIG. 21. Plots of  $x(t)$  (black) and  $y(t)$  (red) for  $d = 0.2, \dots, 0.99$ .

random walk with almost zero probability of reaching either boundary. Between these is a narrow *critical zone*.

In Fig. 22 we plot the  $x(t)$  and  $y(t)$  orbits in the critical zone for  $\tau = 10$ . This extends approximately from  $d = 0.5$  to  $d = 0.64$ . At the lower end of this interval, with probability 0.992, every half-cycle (first return to  $x = 0$ ) includes residence time at one of the boundaries  $x = \pm L$ . The average locking time decreases monotonically as  $d$  increases, and at  $d = 0.64$  the locking probability per half-cycle is down to 0.00161. These probabilities are based on a  $2 \times 10^8$ -step simulation using the algorithm described in the preceding section, with time step 0.002. Event recording was initiated at  $t = 40\,000$  to eliminate dependence on the initial conditions. The orbits plotted in the figure cover the final 10 000 s of the simulation.

Determining precise boundaries of the critical zone is not possible, given the infinite tails of the white noise probability distributions. For practical purposes, empirically determined probability estimates such as those of the preceding paragraph are certainly adequate.

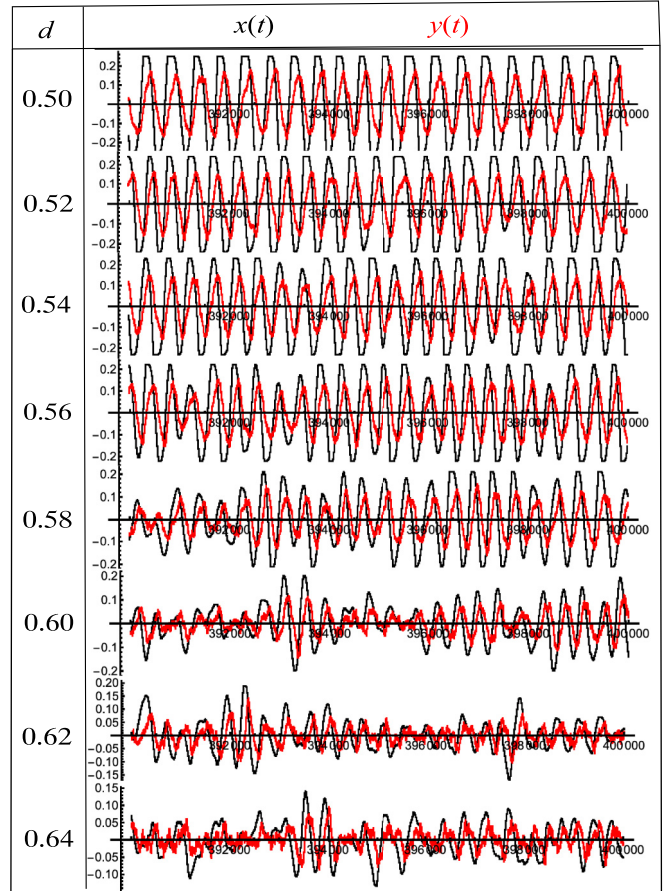


FIG. 22. Plots of  $x(t)$  (black) and  $y(t)$  (red) for  $d = 0.5, \dots, 0.64$ .

To complete our qualitative discussion, we need to return briefly to the extreme values  $d \geq 0.9$ , for which the plate is close to covering the convecting liquid completely. For such  $d$  values, the  $x$  coordinate varies within an interval  $-0.05 \leq x \leq 0.05$ , while the  $y$  excursions are not so constrained. This leads to frequent noise-induced collisions with the boundaries with accompanying locking intervals, as shown in the plot of Fig. 23. This is an interesting departure from the essentially boundary-free motion for smaller supercritical  $d$ , but there is a real question to what extent it can be explored experimentally.

As output of our numerical simulations we record the times of relevant events as they occur. The events are of three types: passage through  $x = 0$  (code 0), arrival at  $x = \pm L$  (code 1), and departure from  $x = \pm L$  (code 2). We store the sequence of event codes, for example,

0, 1, 2, 1, 2, 1, 2, 1, 2, 0, 0, 0, 0, 1, 2, 1, 2, 0, 1, 2,  
1, 2, 1, 2, 0  $\dots$

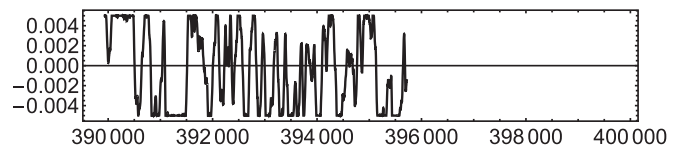


FIG. 23. Plot of  $x(t)$  for  $d = 0.99$ .

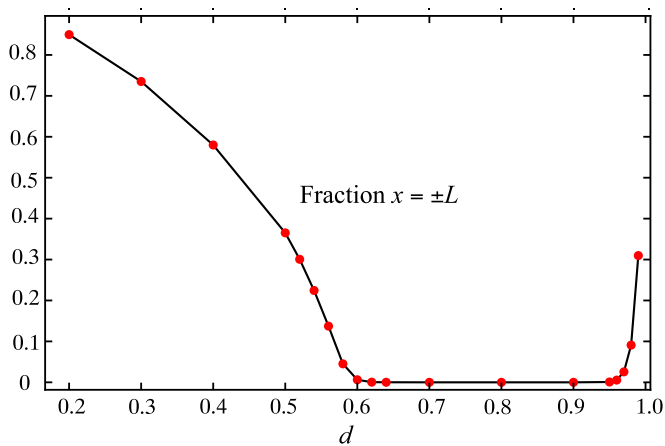


FIG. 24. Fraction of points with  $|x| = \pm L$  as a function of  $d$  for  $\tau = 10$ . The red calculated points have been connected by straight line segments to aid the eye.

Note that the sequence contains a subsequence 0,0,0,0, corresponding to the plate returning to  $x = 0$  several times without making contact with the boundary. This would be typical of a  $d$  value in the critical zone.

A *first return* corresponds to a subsequence 0, (1, 2)<sup>k</sup>, 0 or 0,0. Each subsequence (1, 2) is a *locking interval*, and the subsequence (1, 2)<sup>k</sup> of  $k$  successive locking times sandwiched between two code 0 events is what we will call an *effective locking interval*. In the presence of noise, the departure from the boundary with zero  $x$  velocity is not as simple as in the deterministic model: typically there are noise-induced small excursions from the boundary leading up to a final definitive departure. In such cases,  $k > 1$  and the durations of the excursions are included in the effective locking time.

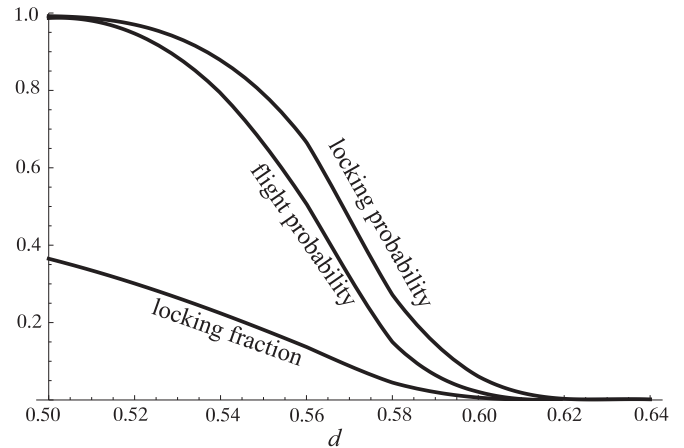


FIG. 25. Plots of locking probability, flight probability, and locking fraction in the critical zone for  $\tau = 10$ .

In our numerical simulations we measure the fraction of time during which the plate is locked at either of the boundaries. The locking fraction as a function of  $d$  is plotted in Fig. 24, based on simulations with  $2 \times 10^8$  time steps of size 0.002.

Figure 25 shows three quantitative measures of the decreased locking in the critical zone. The fall-off of the total locking fraction reflects that the residence times at the boundaries become shorter as well as less frequent as one progresses into the critical zone. The probability that the plate locks at a boundary during any single return to  $x = 0$  is also plotted. The probability of a flight occurring during a single zero-return drops even faster, since a flight, by definition, requires locking during two successive returns.

- 
- [1] J. Zhang and A. Libchaber, Periodic boundary motion in thermal turbulence, *Phys. Rev. Lett.* **84**, 4361 (2000).
- [2] J.-Q. Zhong and J. Zhang, Thermal convection with a freely moving top boundary, *Phys. Fluids* **17**, 115105 (2005).
- [3] J.-Q. Zhong and J. Zhang, Dynamical states of a mobile heat blanket on a thermally convecting fluid, *Phys. Rev. E* **75**, 055301(R) (2007).
- [4] J.-Q. Zhong and J. Zhang, Modeling the dynamics of a free boundary on turbulent thermal convection, *Phys. Rev. E* **76**, 016307 (2007).
- [5] R. Bellman and K. L. Cooke, *Differential-Difference Equations* (Academic Press, New York, NY, 1963).
- [6] P. E. Kloeden, E. Platen, and H. Schurz, *Numerical Solution of SDE through Computer Experiments* (Springer-Verlag, Berlin, 1994).
- [7] J. M. Huang, J.-Q. Zhong, J. Zhang, and L. Mertz, Stochastic dynamics of fluid-structure interaction in turbulent thermal convection, *J. Fluid Mech.* **854**, R5 (2018).
- [8] J. M. Huang, J.-Q. Zhong, J. Zhang, and L. Mertz, Stochastic and deterministic dynamics of a free boundary atop a thermally convecting fluid (unpublished).
- [9] A. Bensoussan and J. Turi, Degenerate Dirichlet problems related to the invariant measure of elasto-plastic Oscillators, *Appl. Math. Optim.* **58**, 1 (2008).
- [10] A. Bensoussan, L. Mertz, O. Pironneau, and J. Turi, An ultra weak finite element method for an elasto-plastic problem with noise, *SIAM J. Numer. Anal.* **47**, 3374 (2009).
- [11] Y. Mao, J.-Q. Zhong, and J. Zhang, The dynamics of an insulating plate over a thermally convecting fluid and its implication for continent movement over convective mantle, *J. Fluid Mech.* **868**, 286 (2019).
- [12] Y. Mao, An insulating plate drifting over a thermally convecting fluid: The effect of plate size on plate motion, coupling modes and flow structure, *J. Fluid Mech.* **916**, A18 (2021).
- [13] Y. Mao, An insulating plate drifting over a thermally convecting fluid: The thermal blanket effect on plume motion and the emergence of a unidirectionally moving mode, *J. Fluid Mech.* **942**, A25 (2022).
- [14] R. L. Devaney, *An Introduction to Chaotic Dynamical Systems* (Benjamin/Cummings Publishing, Menlo Park, CA, 1986).